Research Square

Preprints are preliminary reports that have not undergone peer review.
They should not be considered conclusive, used to inform clinical practice,
or referenced by the media as validated information.

A Glycolipid Metabolism-Related Prognostic Signature and Functional Characterization of SLC35D1 in Colorectal Cancer

Siyu Duan
Nanfang Hospital, Southern Medical University
yan Gu
Nanfang Hospital, Southern Medical University
Yanjun Chen
Nanfang Hospital, Southern Medical University
Xiaolin Li
Nanfang Hospital, Southern Medical University
xinke Wang
wangxinke@smu.edu.cn
Nanfang Hospital, Southern Medical University

Research Article

Keywords: colorectal cancer, glycolipid metabolism, prognostic signature, SLC35D1, DNA methylation, tumor immune microenvironment

Posted Date: November 25th, 2026

DOI: https://doi.org/10.21203/rs.3.rs-11583755/v1

License: This work is licensed under a Creative Commons Attribution 4.0 International License.
Read Full License

Additional Declarations: No competing interests reported.

A Glycolipid Metabolism-Related Prognostic Signature and Functional Characterization of SLC35D1 in Colorectal Cancer

Siyu Duan[1] yanGu[2] Yanjun Chen[3] Xiaolin Li[4] xinke Wang[*]

1 Department of Gastroenterology, Southern Medical University, 1838 Guangzhou North Avenue, Baiyun District, Guangzhou, Guangdong 510515, P.R. China

2 Department of Gastroenterology, Southern Medical University, 1838 Guangzhou North Avenue, Baiyun District, Guangzhou, Guangdong 510515, P.R. China

3 Department of Gastroenterology, Southern Medical University, 1838 Guangzhou North Avenue, Baiyun District, Guangzhou, Guangdong 510515, P.R. China

4 Department of Gastroenterology, Southern Medical University, 1838 Guangzhou North Avenue, Baiyun District, Guangzhou, Guangdong 510515, P.R. China

Corresponding author: Dr xinke Wang

* Department of Gastroenterology, Southern Medical University, 1838 Guangzhou North Avenue, Baiyun District, Guangzhou, Guangdong 510515, P.R. China

Email: wangxinke@smu.edu.cn

Total word count: 8320

Number of figures: 9

Conflict of Interest: The authors declare no conflicts of interest.

Abstract

Background: Molecular heterogeneity limits the prognostic precision of conventional

staging in colorectal cancer (CRC). Although metabolic remodeling and aberrant glycosylation have been implicated in CRC progression, the prognostic relevance of glycolipid metabolism-related genes remains incompletely understood. We aimed to develop a gene-based prognostic signature and characterize the clinical and functional relevance of SLC35D1.

Methods: Transcriptomic and clinical data from The Cancer Genome Atlas (TCGA) and Gene Expression Omnibus (GEO) were integrated with 1,794 candidate genes retrieved from GeneCards. Differential expression analysis, Cox regression, and least absolute shrinkage and selection operator (LASSO) regression were used to develop a prognostic signature, which was evaluated by survival analysis, time-dependent receiver operating characteristic (ROC) curves, external validation, and a clinical nomogram. SLC35D1 was examined using single-cell analysis, clinicopathological associations, immune infiltration estimation, pathway enrichment, computational drug response prediction, and DNA methylation analysis. Overexpression experiments, Western blotting, wound-healing assays, and colony formation assays were used for in vitro evaluation.

Results: Intersecting differentially expressed genes from TCGA and GEO with the candidate gene set identified 70 genes, of which seven were associated with overall survival in univariate Cox analysis. A four-gene signature comprising CD36, MMP3, SLC35D1, and TEX11 stratified patients into groups with significantly different overall survival (log-rank $P < 0.0001$). The 1-, 3-, and 5-year areas under the curve (AUCs) were 0.706, 0.668, and 0.697 in the training cohort, respectively; the reported external-validation AUC was 0.679. The risk score remained associated with overall survival after adjustment for clinical variables (HR = 1.50, 95% CI: 1.14-1.99, P = 0.004). Higher SLC35D1 expression was associated with favorable survival. SLC35D1 also showed associations with estimated immune-cell populations, enriched transcriptional pathways, and methylation at specific CpG sites. In the examined CRC cell models, SLC35D1 overexpression reduced wound closure and colony formation.

Conclusions: The four-gene signature showed moderate prognostic discrimination in CRC. Associations of SLC35D1 with survival, immune infiltration, and CpG methylation, together with its effects on migration-related and clonogenic phenotypes in vitro, support further investigation of its role in CRC. Independent clinical validation and mechanistic experiments are needed before clinical or causal claims can be made.

Keywords: colorectal cancer; glycolipid metabolism; prognostic signature; SLC35D1; DNA methylation; tumor immune microenvironment

1. Introduction

Colorectal cancer (CRC) remains a major global health burden, accounting for approximately 1.93 million new cases and 904,000 deaths in 2022 [1]. Despite advances in screening, surgery, systemic therapies, and immunotherapy, recurrence, metastasis, and treatment resistance continue to limit outcomes [2]. CRC is characterized by marked molecular and clinical heterogeneity, with differences in genomic alterations, transcriptional programs, and tumor microenvironment composition contributing to variable survival even among patients at similar pathological stages [3,4]. Recent molecular profiling has linked these differences to epithelial-mesenchymal transition and metabolic phenotypes [5]. The consensus molecular subtype framework, including the metabolically characterized CMS3 subtype, further illustrates the biological relevance of metabolic variation in CRC [6]. These observations highlight the need for molecular prognostic models that complement conventional clinicopathological risk assessment. Such models should also be evaluated alongside established clinical variables to determine whether their risk estimates provide information beyond tumor stage.

Metabolic reprogramming enables malignant cells to meet the energetic and biosynthetic demands of growth and adaptation. In CRC, altered glucose utilization, fatty acid uptake, lipid synthesis, and mitochondrial metabolism contribute to a complex network of tumor-associated metabolic changes [7-9]. These processes are

interconnected: glucose-derived intermediates support lipid synthesis, whereas lipid availability influences membrane composition and signaling. Metabolic substrates also support the synthesis of nucleotide sugars required for glycosylation, while altered lipid handling may influence stress responses and inflammatory signaling. Metabolites released into the tumor microenvironment can also influence nutrient competition, immune cell activity, and antitumor responses [10]. Furthermore, glucose metabolism provides substrates for glycan biosynthesis, linking metabolic state to the cell-surface glycocalyx and potentially to immune cell function [11]. However, the direction and consequences of metabolic remodeling vary across tumors and cell states. Identifying expression signatures associated with these processes may therefore offer prognostic information without assuming a uniform metabolic program across CRC.

Glycosylation provides an additional connection between cellular metabolism and tumor behavior. Glycan assembly requires coordinated nucleotide sugar synthesis and transport, glycosyltransferase activity, and glycan processing [12]. Aberrant glycosylation can alter receptor behavior, cell adhesion, extracellular signaling, and immune recognition [13], and glycosylation-related enzymes have been implicated in CRC progression [14]. Glycans also contribute to the mechanical properties of the tumor cell surface and its interactions with the extracellular matrix [15]. Their potential roles in immune evasion and checkpoint regulation have stimulated interest in glycosylation-related therapeutic strategies [16,17]. Nevertheless, a broadly defined glycolipid metabolism-related gene set encompasses molecules with distinct functions and does not establish a shared causal pathway. Prognostic associations derived from such a set therefore require careful biological interpretation. This distinction is especially important when candidate genes are selected on the basis of database keyword relevance rather than membership in a functionally validated metabolic pathway.

Among glycan-associated structures, glycosaminoglycans and proteoglycans influence extracellular matrix organization, growth factor presentation, and interactions between tumor and immune cells [18,19]. Their biosynthesis depends in part on nucleotide sugar transport into intracellular secretory compartments [20]. Members of the solute

carrier family 35 (SLC35) contribute to this process, although their substrates and intracellular localization differ [21]. Because extracellular matrix remodeling is implicated in cancer progression and therapeutic responses [22], nucleotide sugar transporters represent candidates for investigating tumor-associated phenotypes. SLC35D1 is particularly relevant because it has reported transport activity toward UDP-glucuronic acid and UDP-N-acetylgalactosamine, both involved in glycosaminoglycan biosynthesis; inherited dysfunction has also been linked to impaired chondroitin sulfate synthesis [21]. Aberrant glycans may influence tumor immune responses [23], including glycan-dependent interactions with inhibitory Siglec receptors [24]. Yet these observations do not establish that SLC35D1 directly regulates immune signaling or specific oncogenic pathways in CRC. Its expression patterns, prognostic relevance, and functional effects therefore warrant direct investigation. The consequences of altered SLC35D1 activity may also depend on substrate availability, cell type, and the surrounding glycan biosynthetic machinery. Importantly, correlations between SLC35D1 expression and DNA methylation or inferred immune-cell populations cannot, by themselves, establish causal regulation.

We integrated TCGA and GEO transcriptomic profiles with candidate glycolipid metabolism-related genes to derive and externally assess a prognostic signature for CRC. We then prioritized SLC35D1 on the basis of its survival association and known involvement in nucleotide sugar transport, and examined its cellular distribution, clinicopathological associations, immune correlates, enriched pathways, DNA methylation, and predicted drug responses. Finally, gain-of-function experiments assessed wound-healing and clonogenic phenotypes. This design connects population-level prognostic associations with preliminary experimental observations without assuming a demonstrated glycosylation-dependent mechanism.

2. Materials and Methods

2.1 Data extraction and analysis

CRC transcriptomic and clinical data were obtained from The Cancer Genome

Atlas (TCGA; https://portal.gdc.cancer.gov/). Overall survival (OS) was the primary endpoint; age, sex, and available TNM characteristics were considered in clinical analyses. Expression and clinical records were matched by sample identifiers, and cases lacking the required survival information were excluded from prognostic analyses.

GSE39582, GSE41258, and GSE44076 were obtained from the Gene Expression Omnibus (https://www.ncbi.nlm.nih.gov/geo/) for differential expression analysis. GSE17536 was used for external prognostic evaluation, and single-cell dataset GSE166555 was used to examine SLC35D1 expression across cell populations. Platform-specific gene annotation and normalization were considered before combining the microarray datasets.

A GeneCards search for "glycolipid metabolism" identified 1,794 candidate genes. Gene identifiers were standardized before intersecting the GeneCards (https://www.genecards.org/) list with TCGA- and GEO-derived differentially expressed genes (DEGs). The study workflow is shown in Figure 1.

2.2 Identification of differentially expressed genes

Microarray data from GSE39582, GSE41258, and GSE44076 were processed by platform and integrated for DEG analysis. Potential dataset-related batch effects were assessed by principal component analysis (PCA) before and after adjustment. Differential expression between CRC and non-tumor tissues was assessed using limma in R [26] for TCGA and integrated GEO expression data. The original DEG criterion was $|\log_2 FC| > 1$ and nominal $P < 0.05$; this threshold should not be interpreted as an adjusted-P-value cutoff. The resulting gene lists were intersected with the GeneCards candidates to identify common genes for survival screening.

2.3 Construction and selection of the glycolipid metabolism-related prognostic model

2.3.1 Identification of prognostic genes

Candidate genes were screened by univariate Cox proportional hazards regression

using TCGA cases with expression and OS data. Genes associated with OS at nominal $P < 0.05$ were entered into least absolute shrinkage and selection operator (LASSO) Cox regression. Coefficient paths and cross-validated partial likelihood deviance were used to examine shrinkage and variable selection. Genes retained by LASSO were entered into a multivariable Cox model to estimate the final signature coefficients.

2.3.2 Risk score calculation

A prognostic risk score was calculated for each patient as the weighted sum of gene expression values and their corresponding multivariate Cox regression coefficients:

$$\text{Risk score} = \Sigma (\beta_i \times \text{Expr}_i)$$

where β_i represents the regression coefficient of gene i, and Expr_i denotes its expression value.

The final four-gene prognostic signature consisted of CD36, MMP3, SLC35D1, and TEX11, with the following risk score formula:

$$\text{Risk score} = 0.2548 \times \text{Expr (CD36)} - 0.1175 \times \text{Expr (MMP3)} - 0.3990 \times \text{Expr (SLC35D1)} - 0.7325 \times \text{Expr (TEX11)}.$$

The calculated risk scores were used for subsequent survival stratification and prognostic evaluation. Positive and negative regression coefficients indicated associations with higher and lower estimated hazards, respectively, conditional on the other genes included in the model.

2.3.3 Evaluation and external validation of the prognostic model

TCGA patients were divided into high- and low-risk groups using the median training-cohort risk score. OS differences were assessed with Kaplan-Meier curves and a log-rank test. Risk distributions, survival-status plots, and expression heatmaps were generated to visualize risk stratification. Time-dependent ROC analysis yielded AUCs at 1, 3, and 5 years.

The fitted four-gene coefficients were retained for prognostic evaluation in the independent GSE17536 cohort. The original external ROC analysis reported an AUC of 0.679; the corresponding prediction time horizon and preprocessing of external expression values require confirmation from the analysis record. The GSE17536 cohort was used for external evaluation of the established four-gene signature. Model performance was assessed using the available survival information and the corresponding risk predictions. The predefined model coefficients were retained for the external evaluation, and the reported ROC results were interpreted according to the prediction time points available from the original analysis.

2.4 Nomogram construction and performance assessment

Univariate and multivariable Cox models evaluated the risk score alongside available clinicopathological variables, including age, sex, and TNM characteristics. A nomogram integrating the risk score with clinical predictors was developed to estimate 1-, 3-, and 5-year OS probabilities. Prognostic discrimination was compared by ROC analysis and time-dependent concordance indices (C-indices). Decision curve analysis (DCA) was used to assess net benefit over selected threshold probabilities. The analyses are shown in Figure 3. Assessment of calibration and incremental performance is needed for a fuller appraisal of clinical usefulness [25].

2.5 Immune microenvironment and functional enrichment analyses

CIBERSORT was used to infer the relative proportions of 22 immune-cell subtypes from bulk transcriptomic profiles [27]. Estimates were compared between risk groups and between high- and low-SLC35D1-expression groups. TIMER2.0 was additionally used to examine SLC35D1-immune-cell associations [28].

Transcriptome-derived immune characteristics, including CAF, CD274, CD8, CTL, T-cell dysfunction and exclusion, IFNG, MDSC, MSI-related score, TAM.M2, and TIDE indicators, were compared between risk groups. These computational features were not interpreted as observed responses to immune checkpoint treatment.

CRC cases were stratified by median SLC35D1 expression for Gene Ontology (GO), Kyoto Encyclopedia of Genes and Genomes (KEGG), and gene set enrichment analysis (GSEA). GSEA used 1,000 permutations, with exploratory enrichment defined as |normalized enrichment score| > 1 and false discovery rate q < 0.25 [29]. The enrichment direction depended on the underlying gene ranking.

2.6 Somatic mutation and DNA methylation analyses

TCGA somatic mutation data in Mutation Annotation Format were summarized using maftools [30]. Mutation frequencies and pathway-associated alterations were described separately in risk groups using cases with available mutation data as denominators. Paired methylation and expression measurements for TCGA-COAD were retrieved through cBioPortal. Associations between SLC35D1 expression and the overall available methylation measure and CpG probes cg09861436 and cg14626797 were assessed using Spearman correlation coefficients and P-values. CpG methylation was represented by β-values.

2.7 Drug response prediction

Drug-response predictions for TCGA CRC cases were generated using GDSC cell-line pharmacogenomic data and the oncoPredict R package [31]. Predicted values for 5-fluorouracil, dasatinib, docetaxel, and teniposide were compared between median-defined SLC35D1-expression groups using Wilcoxon rank-sum tests. These estimates were computational predictions rather than observed treatment outcomes; their direction must be interpreted according to the verified output scale.

2.8 In vitro functional validation

2.8.1 Cell lines and culture conditions

Human CRC cell lines HCT116 (Cat. No. TCHu99) and LOVO (Cat. No. TCHu82), and the non-malignant intestinal epithelial cell line NCM460 were purchased from the Cell Bank of Type Culture Collection (CBTCC, Chinese Academy of Sciences, Shanghai, China), where they were authenticated by short tandem repeat

(STR) profiling prior to distribution. Cells were maintained in complete Dulbecco's modified Eagle medium at 37 °C with 5% CO_2. SLC35D1-overexpressing cells (OE-SLC35D1) were compared with matched empty-vector controls within each cell background. Cell-line provenance, authentication, mycoplasma status, serum concentration, and culture-medium suitability should be documented from laboratory records before submission.

2.8.2 Plasmid transfection

An SLC35D1 overexpression plasmid was obtained from Guangzhou Gidan Biotechnology Co., Ltd. Cells were seeded at approximately 1.2-1.5 × 10^5 cells per well in six-well plates and transfected at approximately 70-80% confluence with Lipofectamine 3000 according to the manufacturer's instructions. RNA and protein were collected approximately 24 and 48 h after transfection, respectively, to confirm overexpression.

2.8.3 RNA extraction and quantitative real-time PCR

Total RNA was extracted using TRIzol, reverse-transcribed into cDNA, and quantified using SYBR Green-based real-time PCR. β-actin served as the reference gene, and relative SLC35D1 expression was estimated with the $2^{-}\Delta\Delta Ct$ method. The reported reverse-transcription conditions were 37 °C for 15 min followed by 85 °C for 5 s, with fivefold dilution of cDNA before PCR. Primer sequences were:

The primer sequences were as follows:

β-actin forward: 5′-AGCGAGCATCCCCCAAAGTT-3′;

β-actin reverse: 5′-GGGCACGAAGGCTCATCATT-3′;

SLC35D1 forward: 5′-AATCCTCCACACTCCGAGATGAG-3′;

SLC35D1 reverse: 5′-GCTCTTATTCACCACCACGATCAG-3′.

Relative expression values were normalized to the corresponding control group for subsequent comparisons.

2.8.4 Western blotting

Cells were lysed in RIPA buffer containing protease inhibitors, and protein concentrations were determined using a bicinchoninic acid assay. Equal protein amounts were separated on 10% SDS-PAGE gels and transferred to PVDF membranes. After blocking in 5% non-fat milk, membranes were incubated overnight at 4 °C with antibodies against SLC35D1 and β-actin, followed by appropriate HRP-conjugated secondary antibodies. Bands were detected by enhanced chemiluminescence and quantified by densitometry, with SLC35D1 normalized to β-actin. Antibody identifiers, dilutions, protein loading amounts, and biological replicate numbers should be added from experimental records.

2.8.5 Wound-healing assay

Following transfection, cells were grown to near confluence in six-well plates. A linear wound was produced with a sterile 200-μL pipette tip, detached cells were removed with PBS, and cultures were maintained in DMEM containing 2% fetal bovine serum. Images from the same regions were collected at 0 and 24 h. Wound closure (%) was calculated as $[(W_0 - W_{24})/W_0] \times 100$, where W denotes wound width measured in ImageJ. Because proliferation can contribute to closure, this assay was interpreted as migration-related rather than migration-specific.

2.8.6 Colony formation assay

Transfected cells were seeded into six-well plates at approximately 1,000 cells per well and cultured for 7-10 days. Colonies were fixed in 4% paraformaldehyde, stained with crystal violet, and counted when they contained at least 50 cells. Colony formation (%) was calculated as (number of colonies/number of seeded cells) × 100. Cell-line identities must be reconciled between the representative photographs and quantitative analysis in Figure 9 before the results are finalized.

2.9 Statistical analysis

Analyses were performed in R (version 4.4.0). Two-group comparisons used

Student's t-tests or Wilcoxon rank-sum tests as appropriate; analysis of variance was used for applicable multi-group comparisons. Pearson or Spearman methods were used for correlations. Survival associations were examined using Kaplan-Meier analysis, log-rank tests, and Cox regression with hazard ratios (HRs) and 95% confidence intervals (CIs). Prognostic performance was summarized using ROC/AUC, time-dependent C-indices, and DCA. The exploratory GSEA FDR criterion is specified above; otherwise $P < 0.05$ was regarded as statistically significant. Numbers of independent biological replicates, multiplicity adjustments, and proportional hazards diagnostics should be reported where available.

Quantitative results from qRT-PCR, Western blotting, wound-healing assays, and colony formation assays were assessed using the available independent experimental replicates. Statistical comparisons were based on replicate-level measurements rather than representative images alone. Unless otherwise specified, $P < 0.05$ was considered statistically significant.

3 Results

3.1 Construction and validation of the glycolipid metabolism-related prognostic signature

To identify glycolipid metabolism-related genes associated with CRC prognosis, three GEO datasets (GSE39582, GSE41258, and GSE44076) were integrated for differential expression analysis. Principal component analysis (PCA) revealed substantial dataset-dependent clustering before batch-effect adjustment. Following adjustment, samples from different datasets exhibited greater overlap, indicating a reduction in detectable batch-associated variation (Figure 2A, B). Differential expression analysis identified 5,513 genes in the TCGA cohort and 590 genes in the integrated GEO datasets. These genes were compared with 1,794 candidate glycolipid metabolism-related genes retrieved from GeneCards. The intersection of all three gene sets yielded 70 common genes, which were retained for subsequent prognostic analyses (Figure 2C).

Univariate Cox regression analysis identified seven genes significantly associated with overall survival (OS): CD36 (HR = 1.259, P = 0.032), CLCA1 (HR = 0.926, P = 0.013), FABP4 (HR = 1.146, P = 0.009), MMP3 (HR = 0.888, P = 0.013), NOTCH3 (HR = 1.269, P = 0.024), SLC35D1 (HR = 0.633, P = 0.005), and TEX11 (HR = 0.372, P = 0.013) (Figure 2D). Among these genes, CD36, FABP4, and NOTCH3 were associated with increased mortality risk, whereas CLCA1, MMP3, SLC35D1, and TEX11 were associated with reduced mortality risk. Subsequent least absolute shrinkage and selection operator (LASSO) regression and cross-validation identified four genes-CD36, MMP3, SLC35D1, and TEX11-for inclusion in the final prognostic signature (Figure 2E, F). CD36 contributed positively to the risk score, whereas MMP3, SLC35D1, and TEX11 had negative coefficients, reflecting their respective associations with estimated mortality risk within the multivariable model.

Using the median risk score as the cutoff, 449 patients in the TCGA training cohort were classified into high-risk (n = 224) and low-risk (n = 225) groups. Kaplan-Meier survival analysis demonstrated significantly shorter OS in the high-risk group than in the low-risk group (log-rank $P < 0.0001$; Figure 2G). Consistently, the distribution of risk scores and survival status showed an increasing concentration of mortality events at higher risk scores. The accompanying expression heatmap revealed distinct patterns across the two risk groups, with CD36 generally exhibiting an expression trend opposite to those of MMP3, SLC35D1, and TEX11 (Figure 2H). Time-dependent ROC analysis yielded AUC values of 0.706, 0.668, and 0.697 for 1-, 3-, and 5-year OS, respectively, indicating moderate prognostic discrimination in the training cohort (Figure 2I). External validation using the independent GSE17536 cohort yielded a reported AUC of 0.679 (Figure 2J). Although the predictive performance was lower than that observed at some time points in the training cohort, the external evaluation suggested that the four-gene signature retained a degree of prognostic discrimination across datasets.

3.2 Construction and evaluation of a prognostic nomogram

To assess the clinical relevance of the four-gene prognostic signature, a nomogram

incorporating the risk score and conventional clinicopathological variables, including age, sex, and T, N, and M stages, was constructed to estimate individual 1-, 3-, and 5-year overall survival (OS) probabilities (Figure 3A). ROC analysis showed that the risk score achieved an AUC of 0.723, compared with 0.576 for age, 0.448 for sex, 0.762 for overall pathological stage, 0.661 for T stage, 0.700 for N stage, and 0.688 for M stage (Figure 3B). These findings indicated that the four-gene signature provided prognostic discrimination comparable to several established clinicopathological indicators, although overall pathological stage showed a higher AUC.

Univariate Cox regression analysis identified significant associations between OS and age, pathological stage, individual TNM components, and the risk score (Figure 3C). After adjustment for the included clinical variables, age (HR = 1.03, 95% CI: 1.01-1.05, P = 0.001), T stage (HR = 2.08, 95% CI: 1.22-3.54, P = 0.007), and the risk score (HR = 1.50, 95% CI: 1.14-1.99, P = 0.004) remained significantly associated with OS (Figure 3D). These results suggest that the four-gene risk score provides prognostic information beyond the clinical variables included in the multivariable model. Time-dependent concordance index (C-index) analysis further characterized the discriminatory performance of the risk score and clinical predictors across follow-up periods (Figure 3E). Decision curve analysis (DCA) demonstrated differences in net benefit among the evaluated prediction models across selected threshold probabilities (Figure 3F), suggesting potential clinical utility that warrants further validation. Collectively, these findings support the independent prognostic association of the four-gene signature and its potential value as a complementary component of CRC survival prediction.

3.3 Immune characteristics and somatic mutation profiles of the risk groups

To investigate the biological characteristics associated with the four-gene prognostic signature, we compared immune infiltration patterns and somatic mutation profiles between the high- and low-risk groups. CIBERSORT analysis revealed differences in the relative proportions of several immune cell populations, particularly

$CD4^+$ memory T-cell and macrophage subsets (Figure 4A). The high-risk group exhibited a tendency toward increased M2-like macrophage infiltration, suggesting differences in the immune composition of the two risk groups. Further analysis of immune-related indicators, including CAF, CD274, CD8, CTL, T-cell dysfunction, T-cell exclusion, IFNG, MSI-related scores, TAM.M2, and TIDE, identified significant differences in several transcriptome-derived immune characteristics between the groups (Figure 4B). These findings indicate distinct immune-associated profiles across the prognostic risk groups.

Somatic mutation-associated pathway analysis was subsequently performed to characterize the molecular alterations underlying the risk groups. Both groups exhibited mutations affecting several cancer-related signaling pathways, including RTK-RAS, WNT, NOTCH, Hippo, PI3K, MYC, cell cycle, TGF-β, TP53, and NRF2 pathways (Figure 4C, D). Although the overall pathway profiles were broadly comparable, differences were observed in the proportions of pathway-associated genes and samples harboring mutations. RTK-RAS and WNT were among the prominently affected pathways in both groups, indicating shared mutational characteristics despite their different prognostic classifications.

Somatic mutation landscape analysis included 209 high-risk and 201 low-risk patients with available mutation data (Figure 4E, F). APC was the most frequently mutated gene in both groups, with a mutation frequency of 72%. TP53 and KRAS mutations were observed in 59% and 45% of high-risk patients, respectively, compared with 52% and 41% of low-risk patients. Conversely, PIK3CA mutations occurred in 26% of high-risk patients and 32% of low-risk patients. Other frequently altered genes included TTN and several additional genes identified in the mutation profiles. These results reveal descriptive differences in mutation frequencies between the risk groups, although the statistical significance of these differences was not established. Collectively, the immune infiltration and somatic mutation analyses identified distinct biological characteristics associated with the four-gene prognostic signature, providing additional context for the observed differences in patient survival.

3.4 Expression patterns and prognostic significance of SLC35D1 in CRC

Among the four genes included in the prognostic signature, SLC35D1 was selected for further investigation because of its association with favorable survival outcomes, established involvement in nucleotide sugar transport, and relatively limited functional characterization in CRC. Single-cell RNA sequencing analysis of the GSE166555 dataset revealed distinct cell populations within the CRC microenvironment, including epithelial, malignant, and various stromal and immune cell populations (Figure 5A). SLC35D1 expression was predominantly distributed among epithelial-associated cell clusters, although detectable expression was also observed in other cell populations (Figure 5B). These findings suggest that SLC35D1 expression is associated with epithelial cell populations in CRC. Analysis of paired CRC and adjacent normal tissues revealed significantly lower SLC35D1 expression in tumor tissues (Figure 5C). Pan-cancer expression analysis further demonstrated heterogeneous SLC35D1 expression patterns across different malignancies, suggesting that its expression characteristics may be tumor-type dependent.

To evaluate its potential diagnostic relevance, ROC analysis was performed using 514 samples, including 473 CRC and 41 normal tissue samples. SLC35D1 achieved an AUC of 0.936, while the combined four-gene signature yielded an AUC of 0.999 (Figure 5D). These results indicate strong discrimination between tumor and normal samples within the analyzed dataset, although the diagnostic performance requires independent validation. Kaplan-Meier survival analysis demonstrated that patients with higher SLC35D1 expression had significantly better overall survival than those with lower expression (HR = 0.56, log-rank P = 0.019; Figure 5E). This association was consistent with the negative regression coefficient of SLC35D1 in the four-gene prognostic model.

Further analysis of clinicopathological characteristics showed that SLC35D1 expression differed across pathological stages. Lower expression was observed in T3

tumors than in T2 tumors, while significant differences were also identified among pathological stage groups (Figure 5F, G). Comparison of M0, M1, and normal tissue groups revealed higher SLC35D1 expression in normal tissues, without a consistent decrease between M0 and M1 tumors (Figure 5H). Collectively, these findings demonstrate that reduced SLC35D1 expression is associated with CRC tissues and certain clinicopathological characteristics, whereas higher expression is associated with improved overall survival. Together with its epithelial-associated expression pattern, these observations support further investigation of the biological role of SLC35D1 in CRC.

3.5 Association between SLC35D1 expression and immune cell infiltration in CRC

To investigate the relationship between SLC35D1 expression and the tumor immune microenvironment, immune cell infiltration patterns were analyzed using CIBERSORT. The estimated proportions of immune cell populations varied across CRC samples, with differences observed between the high- and low-SLC35D1-expression groups (Figure 6A, B). Correlation analysis further revealed that SLC35D1 expression was positively associated with several immune cell subsets, including resting $CD4^+$ memory T cells, activated dendritic cells, naïve B cells, and plasma cells. In contrast, negative correlations were observed with M0 and M1 macrophages and certain natural killer (NK) cell populations (Figure 6C).

Further analyses of selected immune cell populations showed that SLC35D1 expression was negatively correlated with NK cells ($R = -0.20$, $P = 1.5 \times 10^{-5}$) and M1 macrophages ($R = -0.27$, $P = 2.5 \times 10^{-9}$) (Figure 6D, E). Conversely, positive correlations were observed with plasma cells ($R = 0.17$, $P = 1.3 \times 10^{-4}$) and naïve B cells ($R = 0.19$, $P = 3.3 \times 10^{-5}$) (Figure 6F, G). Although these associations were statistically significant, their relatively modest correlation coefficients indicated limited to moderate effect sizes.

Collectively, these findings demonstrate that SLC35D1 expression is associated with distinct immune infiltration patterns in CRC, suggesting a potential relationship

between SLC35D1-associated molecular characteristics and the tumor immune microenvironment.

3.6 Functional enrichment analysis of SLC35D1-associated genes in CRC

To explore the biological processes associated with SLC35D1 expression in CRC, Gene Ontology (GO), Kyoto Encyclopedia of Genes and Genomes (KEGG), and gene set enrichment analyses (GSEA) were performed. GO enrichment analysis revealed that SLC35D1-associated genes were predominantly enriched in processes related to ribonucleoprotein complex biogenesis, chromosome segregation, ribosome biogenesis, rRNA processing, and mitotic nuclear division (Figure 7A). These findings suggest that SLC35D1 expression is associated with transcriptional programs involved in cellular proliferation, chromosome organization, and protein biosynthesis. KEGG pathway analysis identified enrichment in several cancer-associated signaling and cellular regulatory pathways, including PI3K-Akt signaling, Wnt signaling, extracellular matrix (ECM)-receptor interaction, regulation of the actin cytoskeleton, Th17 cell differentiation, and sphingolipid signaling (Figure 7B). These pathways are involved in diverse biological processes, including cell growth, adhesion, cytoskeletal organization, and immune regulation.

GSEA further revealed distinct enrichment patterns across metabolic and immune-related gene sets (Figure 7C). Positive normalized enrichment scores (NESs) were observed for pathways associated with fatty acid degradation, peroxisomal function, retinol metabolism, and phosphatidylinositol signaling. In contrast, oxidative phosphorylation, cell adhesion molecules, chemokine signaling, antigen processing and presentation, and several immune-related pathways exhibited negative NESs. These findings indicate coordinated differences in metabolic, adhesion-related, and immune-associated transcriptional programs across the analyzed expression profiles. Furthermore, the functional association chord diagram illustrated connections between SLC35D1-associated genes and multiple GO categories, including cell-cell signaling, cell junction organization, natural killer cell degranulation, and endosomal membrane-

related processes (Figure 7D). Collectively, these enrichment analyses suggest that SLC35D1 expression is associated with biological networks involving cell proliferation, metabolism, intercellular interactions, and immune-related functions, providing a basis for further mechanistic investigation.

3.7 Associations of SLC35D1 expression with predicted drug responses and DNA methylation in CRC

To investigate the potential relationship between SLC35D1 expression and therapeutic response, drug response predictions were performed using GDSC-derived pharmacogenomic data. Significant differences in predicted response values were observed between the high- and low-SLC35D1-expression groups for 5-fluorouracil ($P = 7.2 \times 10^{-5}$), dasatinib ($P = 5.9 \times 10^{-11}$), docetaxel ($P = 5.2 \times 10^{-5}$), and teniposide ($P = 3.1 \times 10^{-7}$) (Figure 8A-D). For all four drugs, the high-SLC35D1-expression group exhibited higher predicted response values than the low-expression group. These findings indicate an association between SLC35D1 expression and computationally estimated drug responses. However, the direction of drug sensitivity cannot be determined without confirming the scale and interpretation of the prediction outputs.

To further explore potential epigenetic associations with SLC35D1 expression, DNA methylation profiles were analyzed using matched transcriptomic and methylation data from the TCGA-COAD cohort. An inverse correlation was observed between the overall SLC35D1 methylation measure and its mRNA expression ($\rho = -0.36$, $P = 1.6 \times 10^{-10}$; Figure 8E). Site-specific analyses further revealed a significant negative correlation between methylation at cg09861436 and SLC35D1 expression ($\rho = -0.377$, $P < 0.0001$; Figure 8F). A weaker but statistically significant negative correlation was also identified at cg14626797 ($\rho = -0.16$, $P = 0.0048$; Figure 8G). These results demonstrate that SLC35D1 expression is associated with distinct computational drug response profiles and inversely correlated with DNA methylation at specific CpG sites in CRC. The observed methylation-expression associations suggest a potential epigenetic relationship that warrants further functional investigation.

3.8 SLC35D1 overexpression suppresses migration-related and clonogenic phenotypes in CRC cells

To investigate the functional relevance of SLC35D1 in CRC, its basal expression was first examined in CRC cell lines and normal intestinal epithelial control cells. Quantitative real-time PCR analysis revealed lower SLC35D1 mRNA expression in HCT116 and LOVO cells than in the corresponding normal reference conditions (Figure 9A). Consistently, Western blot analysis showed reduced SLC35D1 protein expression in the examined tumor cells (Figure 9B). These findings were consistent with the tissue expression patterns observed in the transcriptomic analysis. To further evaluate the effects of SLC35D1 on CRC cell behavior, SLC35D1-overexpressing cell models were established. Western blot analysis confirmed increased SLC35D1 protein expression following plasmid transfection in HCT116 and LOVO cells compared with their respective vector controls (Figure 9C, D), supporting the successful establishment of the overexpression conditions for subsequent functional assays.

Wound-healing assays were performed to assess migration-related cellular behavior. After 24 h, SLC35D1-overexpressing HCT116 and LOVO cells exhibited reduced wound closure compared with the corresponding negative control groups (Figure 9E, F). The differences were reported to be statistically significant ($P < 0.05$), suggesting that SLC35D1 overexpression attenuated wound-healing capacity in both cell models. The effect of SLC35D1 overexpression on clonogenic growth was subsequently examined using colony formation assays. Representative images showed fewer colonies in SLC35D1-overexpressing HCT116 and LOVO cells than in their respective controls (Figure 9G). Quantitative analysis further demonstrated significantly reduced colony numbers in the SLC35D1-overexpressing groups of RKO and LOVO cells (Figure 9H). Together, these findings indicate that elevated SLC35D1 expression is associated with reduced clonogenic capacity in the examined CRC cell models. Collectively, the expression analyses and functional assays provide initial experimental evidence that SLC35D1 overexpression suppresses wound closure and colony formation in CRC cells, supporting its potential growth-restrictive role in CRC.

4 Discussion

This study combined prognostic modeling, public-transcriptome analyses, and in vitro experiments to investigate glycolipid metabolism-related genes in CRC. A four-gene signature was associated with overall survival, and SLC35D1 was prioritized for further characterization. The combined evidence supports a potential association between SLC35D1 and CRC-related cellular phenotypes but does not establish a causal pathway linking nucleotide sugar transport, epigenetic alterations, immune activity, and cancer progression.

The prognostic signature comprised CD36, MMP3, SLC35D1, and TEX11, which represent distinct biological processes rather than a single established metabolic pathway. CD36 is involved in fatty acid uptake and has been implicated in lipid-associated colorectal tumor progression [32]. MMP3 belongs to the matrix metalloproteinase family, whose members participate in extracellular matrix remodeling, a process associated with CRC progression and immune microenvironment heterogeneity [33]. SLC35D1 is involved in nucleotide sugar transport, whereas TEX11 is primarily characterized in meiotic processes. The combined signature significantly stratified patients according to overall survival, with an external validation AUC of 0.679, indicating moderate prognostic discrimination. Multivariate analysis further supported an independent association between the risk score and survival. However, statistical independence does not necessarily demonstrate improved performance beyond conventional clinical predictors. Recent CRC nomogram studies have emphasized the importance of assessing discrimination, calibration, and clinical net benefit [34]. As the present analyses did not include complete calibration assessment, further validation is required before clinical implementation.

SLC35D1 was prioritized because it was associated with survival and is known to transport nucleotide sugars relevant to glycosaminoglycan biosynthesis [20,21]. Glycosaminoglycans and proteoglycans can influence extracellular matrix organization and cell-matrix interactions [18,19]. CRC studies have also demonstrated subtype-

dependent extracellular matrix composition and tumor-promoting remodeling processes [35,36]. These observations offer a rationale for mechanistic studies; however, glycosaminoglycan abundance, nucleotide sugar transport, and extracellular matrix remodeling were not directly measured here. Their involvement in the observed CRC phenotypes therefore remains hypothetical.

Several observations support a potential growth-restrictive role for SLC35D1 in CRC. Its expression was reduced in paired tumor tissues and selected CRC cell models, whereas higher expression was associated with improved survival. Single-cell analysis further revealed SLC35D1 expression predominantly in epithelial-associated populations. Importantly, SLC35D1 overexpression reduced wound closure and colony formation in the examined CRC cells. These findings provide initial functional evidence beyond observational survival associations. Nevertheless, wound-healing assays cannot completely distinguish migration from proliferation, and clonogenic assays do not identify the molecular processes responsible for reduced colony formation. Reciprocal knockdown, rescue experiments, and in vivo validation are therefore necessary to determine whether SLC35D1 consistently restricts malignant phenotypes across different CRC molecular backgrounds.

Functional enrichment analyses revealed associations between SLC35D1 expression and pathways involved in cell division, ribosome biogenesis, cytoskeletal organization, extracellular matrix interactions, and metabolic regulation. PI3K-Akt and Wnt signaling were also represented among the enriched pathways. These pathways contribute to CRC growth, survival, and therapeutic resistance, with PI3K-Akt signaling receiving considerable attention as a potential therapeutic target [37]. However, enrichment reflects coordinated transcriptional associations rather than direct pathway regulation. The present study did not assess AKT phosphorylation, β-catenin localization, or glycosylation of specific signaling proteins. Future studies combining SLC35D1 perturbation with glycosaminoglycan profiling and pathway activity measurements may help establish whether the observed transcriptional associations reflect functional regulatory relationships.

Immune infiltration analyses identified correlations between SLC35D1 expression and several immune cell populations, including B cells, plasma cells, $CD4^+$ memory T cells, natural killer cells, and macrophage subsets. The CRC immune microenvironment is highly heterogeneous, and the biological consequences of immune infiltration depend on cellular localization, functional state, and interactions with surrounding tissues [38]. Spatial multi-omics studies have further demonstrated that macrophage-T-cell interactions form distinct immune niches associated with treatment-related phenotypes [39]. Accordingly, the mixed positive and negative correlations observed in the present study do not support a generalized conclusion that SLC35D1 enhances antitumor immunity. Furthermore, transcriptomic deconvolution estimates cellular composition rather than directly measuring immune function. Recent benchmarking studies have demonstrated variability in the performance of computational deconvolution methods, particularly for specific immune cell states [40]. Multiplex immunostaining, spatial transcriptomics, and tumor-immune co-culture experiments would therefore be valuable for determining whether SLC35D1 contributes to immune microenvironment regulation.

DNA methylation analysis revealed an inverse relationship between SLC35D1 expression and methylation levels, including negative correlations at cg09861436 and cg14626797. DNA methylation can influence gene expression through context-dependent changes in chromatin organization and transcriptional regulation, while also interacting with the tumor immune microenvironment [41]. However, methylation-expression correlations may reflect differences in cellular composition or other molecular characteristics rather than direct transcriptional silencing. A systematic review and external validation study of CpG-based prognostic biomarkers in CRC also highlighted the challenges of establishing reproducible clinical value from methylation-associated signatures [42]. Because the functional genomic positions of the investigated CpG probes were not independently verified and methylation perturbation experiments were not performed, the present results should be interpreted as evidence of methylation-associated expression variation rather than confirmed promoter

hypermethylation-mediated suppression. Targeted epigenetic perturbation and subsequent expression analysis would help clarify this relationship.

Computational drug response analysis identified significant associations between SLC35D1 expression and predicted responses to 5-fluorouracil, dasatinib, docetaxel, and teniposide. Notably, predicted response values were higher in the SLC35D1-high group. If these values represent IC50 or its logarithmic transformation, higher values generally correspond to reduced drug sensitivity. Therefore, the prediction metric must be verified before assigning a biological direction to these differences. Importantly, computational predictions based on pharmacogenomic training data do not constitute direct evidence of clinical treatment benefit. Studies using patient-derived CRC organoids have demonstrated the feasibility of linking experimentally measured drug responses with clinical outcomes, while emphasizing the need for appropriate testing frameworks [43]. Additional work has shown that IC50-based classifications require clinical calibration to support meaningful sensitivity thresholds [44]. More recent prospective organoid investigations have further explored the relationship between ex vivo drug sensitivity and treatment outcomes in metastatic CRC [45]. These studies highlight the experimental and clinical validation required before SLC35D1-associated drug response estimates can be considered therapeutically informative.

This study has several limitations. The initial candidate list was derived from GeneCards keyword retrieval and may include genes without a demonstrated role in glycolipid metabolism. The transcriptomic analyses were susceptible to platform and cohort heterogeneity, and prognostic discrimination was moderate. Details of internal validation, calibration, external preprocessing, and time-specific external AUCs require complete documentation. The near-perfect tumor-versus-normal ROC result should be examined for overfitting or data leakage. Immune deconvolution, enrichment, drug-response prediction, and methylation analyses were observational or computational; no causal epigenetic or immune mechanism was established. Finally, cell-based evidence was limited to overexpression experiments without reciprocal knockdown, rescue, or in vivo validation, and the colony-formation panels require reconciliation of cell-line

identities.

In conclusion, the four-gene signature showed moderate prognostic discrimination in CRC. SLC35D1 expression was associated with survival, estimated immune infiltration, and CpG methylation, whereas SLC35D1 overexpression reduced wound closure and colony formation in vitro. These findings justify further mechanistic studies and independent clinical validation but do not yet support clinical implementation.

Author Contributions

Siyu Duan: Conceptualization and methodology. Yanjun Chen: Formal analysis, data interpretation, and writing - review and editing. Xiaolin Li: Writing - original draft and experimental data organization. Yan Gu and Xinke Wang: Supervision and manuscript review. All authors contributed to the manuscript and read and approved the final version.

Funding

This research was supported by the project "Construction and Demonstration Application of an Early Warning System for Gastric Cancer Progression Based on Integrated Traditional Chinese and Western Medicine" (Grant No. NFEC-2025-522).

Conflict of Interest

The authors declare that the research was conducted in the absence of any commercial or financial relationships that could be construed as a potential conflict of interest.

Ethics and consent to participate declarations

Not applicable. This study involved secondary analyses of publicly available, de-identified patient datasets and in vitro cell experiments. No new participants were recruited, and no identifiable individual information is presented.

Availability of data and materials

Transcriptomic and clinical data of the TCGA-COAD cohort were downloaded from

the Genomic Data Commons (GDC): https://portal.gdc.cancer.gov/projects/TCGA-COAD. Validation datasets were obtained from the GEO repository: GSE39582 (https://www.ncbi.nlm.nih.gov/geo/query/acc.cgi?acc=GSE39582),GSE41258 (https://www.ncbi.nlm.nih.gov/geo/query/acc.cgi?acc=GSE41258),GSE44076 (https://www.ncbi.nlm.nih.gov/geo/query/acc.cgi?acc=GSE44076),GSE17536 (https://www.ncbi.nlm.nih.gov/geo/query/acc.cgi?acc=GSE17536), and GSE166555 (https://www.ncbi.nlm.nih.gov/geo/query/acc.cgi?acc=GSE166555). Gene annotation information of SLC35D1 was retrieved from GeneCards: https://www.genecards.org/cgi-bin/carddisp.pl?gene=SLC35D1. Somatic mutation data for colorectal cancer was analyzed via cBioPortal: https://www.cbioportal.org/study?id=coadread_tcga_pan_can_atlas_2018. Immune infiltration analysis was performed using TIMER2.0: http://timer.cistrome.org/. Drug response data were obtained from the Genomics of Drug Sensitivity in Cancer (GDSC) database: https://www.cancerrxgene.org/.

Consent to publication

Not applicable

Acknowledgements

We acknowledge Nanfang hospital for offering access to its research platform, experimental facilities and technical environment for sample processing and laboratory testing. We are grateful to the team members of the hospital's research platform for their technical guidance during the experiments.

Reference

[1] Bray F, Laversanne M, Sung H, Ferlay J, Siegel RL, Soerjomataram I, et al. Global cancer statistics 2022: GLOBOCAN estimates of incidence and mortality worldwide for 36 cancers in 185 countries. CA Cancer J Clin. (2024) 74:229-63. doi: 10.3322/caac.21834

[2] Siegel RL, Wagle NS, Cercek A, Smith RA, Jemal A. Colorectal cancer statistics, 2023. CA Cancer J Clin. (2023) 73:233-54. doi: 10.3322/caac.21772

[3] Dunne PD, Arends MJ. Molecular pathological classification of colorectal cancer-an update. Virchows Arch. (2024) 484:273-85. doi: 10.1007/s00428-024-03746-3

[4] Shin AE, Giancotti FG, Rustgi AK. Metastatic colorectal cancer: mechanisms and emerging therapeutics. Trends Pharmacol Sci. (2023) 44:222-36. doi: 10.1016/j.tips.2023.01.003

[5] Sehgal M, Ramu S, Vaz JM, Ganapathy YR, Muralidharan S, Venkatraghavan S, et al. Characterizing heterogeneity along EMT and metabolic axes in colorectal cancer reveals underlying consensus molecular subtype-specific trends. Transl Oncol. (2024) 40:101845. doi: 10.1016/j.tranon.2023.101845

[6] Kantha A, Das D, Pai E, Kumar T, Pandey M. Consensus molecular subtypes (CMS) classification: a progress towards subtype-driven treatments in colorectal cancer. World J Surg Oncol. (2026) 24:1. doi: 10.1186/s12957-025-04117-1

[7] Zhang J, Zou S, Fang L. Metabolic reprogramming in colorectal cancer: regulatory networks and therapy. Cell Commun Signal. (2023) 21:25. doi: 10.1186/s13578-023-00977-w

[8] Zhou R, Wang F, Wen J, Zhou X, Wen Y. Glucose metabolic reprogramming in colorectal cancer: from mechanisms to targeted therapy approaches. Cancer Med. (2025) 14. doi: 10.1002/cam4.71185

[9] Liu W, Dong S, Hao F, Gao Y, Wei Q. Lipid metabolic reprogramming in colorectal cancer: mechanisms and therapeutic strategies. Front Immunol. (2025) 16:1603032. doi: 10.3389/fimmu.2025.1603032

[10] De Martino M, Rathmell JC, Galluzzi L, Vanpouille-Box C. Cancer cell

metabolism and antitumour immunity. Nat Rev Immunol. (2024) 24:654-69. doi: 10.1038/s41577-024-01026-4
[11]Schuurmans F, Wagemans KE, Adema GJ, Cornelissen LAM. Tumor glucose metabolism and the T cell glycocalyx: implication for T cell function. Front Immunol. (2024) 15:1409238. doi: 10.3389/fimmu.2024.1409238
[12]Stanley P. Genetics of glycosylation in mammalian development and disease. Nat Rev Genet. (2024) 25:715-29. doi: 10.1038/s41576-024-00725-x
[13]Cao Y, Yi W, Zhu Q. Glycosylation in the tumor immune response: the bitter side of sweetness. Acta Biochim Biophys Sin (Shanghai). (2024) 56:1184-98. doi: 10.3724/abbs.2024107
[14]Tian H, Yu JL, Chu X, Guan Q, Liu J, Liu Y. Unraveling the role of C1GALT1 in abnormal glycosylation and colorectal cancer progression. Front Oncol. (2024) 14:1389713. doi: 10.3389/fonc.2024.1389713
[15]Purushothaman A, Mohajeri M, Lele TP. The role of glycans in the mechanobiology of cancer. J Biol Chem. (2023) 299:102935. doi: 10.1016/j.jbc.2023.102935
[16]Ren X, Lin S, Guan F, Kang H. Glycosylation targeting: a paradigm shift in cancer immunotherapy. Int J Biol Sci. (2024) 20:2607-21. doi: 10.7150/ijbs.93806
[17]Zheng L, Yang Q, Li F, Zhu M, Yang H, Tan T, et al. The glycosylation of immune checkpoints and their applications in oncology. Pharmaceuticals (Basel). (2022) 15:1451. doi: 10.3390/ph15121451
[18]Wieboldt R, Läubli H. Glycosaminoglycans in cancer therapy. Am J Physiol Cell Physiol. (2022) 322-C1200. doi: 10.1152/ajpcell.00063.2022
[19]Deb G, Cicala A, Papadas A, Asimakopoulos F. Matrix proteoglycans in tumor inflammation and immunity. Am J Physiol Cell Physiol. (2022) 323-C693. doi: 10.1152/ajpcell.00023.2022
[20]Maszczak-Seneczko D, Wiktor M, Skurska E, Wiertelak W, Olczak M. Delivery of nucleotide sugars to the mammalian Golgi: a very well (un)explained story. Int J Mol Sci. (2022) 23:8648. doi: 10.3390/ijms23158648
[21]Kamiyama S, Sone H. Solute carrier family 35 (SLC35)-an overview and recent progress. Biologics. (2024) 4:242-79. doi: 10.3390/biologics4030017
[22]He X, Lee B, Jiang Y. Extracellular matrix in cancer progression and therapy. Med Rev. (2022) 2:125-39. doi: 10.1515/mr-2021-0028
[23]Matsumoto Y, Ju T. Aberrant glycosylation as immune therapeutic targets for solid tumors. Cancers (Basel). (2023) 15:3536. doi: 10.3390/cancers15143536
[24]Mantuano NR, Läubli H. Sialic acid and Siglec receptors in tumor immunity and immunotherapy. Semin Immunol. (2024) 74-75:101893. doi: 10.1016/j.smim.2024.101893
[25]Collins GS, Moons KGM, Dhiman P, Riley RD, Beam AL, Van Calster B, et al. TRIPOD+AI statement: updated guidance for reporting clinical prediction models that use regression or machine learning methods. BMJ. (2024) 385. doi: 10.1136/bmj-2023-078378
[26]Ritchie ME, Phipson B, Wu D, Hu Y, Law CW, Shi W, et al. limma powers differential expression analyses for RNA-sequencing and microarray studies. Nucleic

Acids Res. (2015) 43. doi: 10.1093/nar/gkv007
[27]Newman AM, Liu CL, Green MR, Gentles AJ, Feng W, Xu Y, et al. Robust enumeration of cell subsets from tissue expression profiles. Nat Methods. (2015) 12:453-7. doi: 10.1038/nmeth.3337
[28]Li T, Fu J, Zeng Z, Cohen D, Li J, Chen Q, et al. TIMER2.0 for analysis of tumor-infiltrating immune cells. Nucleic Acids Res. (2020) 48-W514. doi: 10.1093/nar/gkaa407
[29]Subramanian A, Tamayo P, Mootha VK, Mukherjee S, Ebert BL, Gillette MA, et al. Gene set enrichment analysis: a knowledge-based approach for interpreting genome-wide expression profiles. Proc Natl Acad Sci USA. (2005) 102:15545-50. doi: 10.1073/pnas.0506580102
[30]Mayakonda A, Lin DC, Assenov Y, Plass C, Koeffler HP. Maftools: efficient and comprehensive analysis of somatic variants in cancer. Genome Res. (2018) 28:1747-56. doi: 10.1101/gr.239244.118
[31]Maeser D, Gruener RF, Huang RS. oncoPredict: an R package for predicting in vivo or cancer patient drug response and biomarkers from cell line screening data. Brief Bioinform. (2021) 22. doi: 10.1093/bib/bbab260
[32]Li B, Mi J, Yuan Q. Fatty acid metabolism-related enzymes in colorectal cancer metastasis: from biological function to molecular mechanism. Cell Death Discov. (2024) 10:350. doi: 10.1038/s41420-024-02126-9
[33]Chen W, Wang Y, Gu H, Zhang Y, Chen C, Yu T, et al. Molecular characteristics, clinical significance, and immune landscape of extracellular matrix remodeling-associated genes in colorectal cancer. Front Oncol. (2023) 13:1109181. doi: 10.3389/fonc.2023.1109181
[34]Yin W, Pei W, Yu T, Zhang Q, Zhang S, Zhang M, et al. Construction and validation of a nomogram for predicting overall survival of patients with stage III/IV early-onset colorectal cancer. Front Oncol. (2024) 14:1332499. doi: 10.3389/fonc.2024.1332499
[35]Lee HJ, Park SW, Lee JH, Chang SY, Oh SM, Mun S, et al. Differential cellular origins of the extracellular matrix of tumor and normal tissues according to colorectal cancer subtypes. Br J Cancer. (2025) 132:770-82. doi: 10.1038/s41416-025-02964-z
[36]Lee CJ, Jang TY, Jeon SE, Yun HJ, Cho YH, Lim DY, et al. The dysadherin/MMP9 axis modifies the extracellular matrix to accelerate colorectal cancer progression. Nat Commun. (2024) 15:10422. doi: 10.1038/s41467-024-54920-9
[37]Leiphrakpam PD, Are C. PI3K/Akt/mTOR signaling pathway as a target for colorectal cancer treatment. Int J Mol Sci. (2024) 25:3178. doi: 10.3390/ijms25063178
[38]Kennel KB, Greten FR. The immune microenvironment of colorectal cancer. Nat Rev Cancer. (2025) 25:945-64. doi: 10.1038/s41568-025-00872-1
[39]Zhang H, Hong L, Dong Z, Xin S, Lin B, Cheng J, et al. Spatially resolved C1QC+ macrophage-CD4+ T cell niche in colorectal cancer microenvironment: implications for immunotherapy response. Cell Discov. (2025) 11:60. doi: 10.1038/s41421-025-00811-2
[40]White BS, de Reyniès A, Newman AM, Waterfall JJ, Lamb A, Petitprez F, et al. Community assessment of methods to deconvolve cellular composition from bulk gene expression. Nat Commun. (2024) 15:7362. doi: 10.1038/s41467-024-50618-0

[41] Zhu D, Zeng S, Su C, Li J, Xuan Y, Lin Y, et al. The interaction between DNA methylation and tumor immune microenvironment: from the laboratory to clinical applications. Clin Epigenetics. (2024) 16:24. doi: 10.1186/s13148-024-01633-x
[42] Yuan T, Edelmann D, Kather JN, Fan Z, Tagscherer KE, Roth W, et al. CpG-biomarkers in tumor tissue and prediction models for the survival of colorectal cancer: a systematic review and external validation study. Crit Rev Oncol Hematol. (2024) 193:104199. doi: 10.1016/j.critrevonc.2023.104199
[43] Tan T, Mouradov D, Lee M, Gard G, Hirokawa Y, Li S, et al. Unified framework for patient-derived, tumor-organoid-based predictive testing of standard-of-care therapies in metastatic colorectal cancer. Cell Rep Med. (2023) 4:101335. doi: 10.1016/j.xcrm.2023.101335
[44] Tang Y, Wang T, Hu Y, Ji H, Yan B, Hu X, et al. Cutoff value of IC50 for drug sensitivity in patient-derived tumor organoids in colorectal cancer. iScience. (2023) 26:107116. doi: 10.1016/j.isci.2023.107116
[45] Smabers LP, Wensink GE, Verissimo CS, Doorn M, Yang T, Voskuilen T, et al. Patient-derived organoids predict treatment response in metastatic colorectal cancer. Clin Cancer Res. (2025) 31:5015-26. doi: 10.1158/1078-0432.CCR-25-1564

Figure legends:

Figure 1. Overview of the study design and analytical workflow. Schematic illustration of dataset integration, identification of glycolipid metabolism-related genes, prognostic model development and validation, and bioinformatic and experimental characterization of SLC35D1 in colorectal cancer (CRC).

Figure 2. Identification of prognostic glycolipid metabolism-related genes and development and validation of a four-gene prognostic signature in CRC. (A, B) PCA plots before and after batch-effect adjustment. (C) Venn diagram showing the intersection of TCGA-derived DEGs, GEO-derived DEGs, and candidate glycolipid metabolism-related genes. (D) Univariate Cox regression analysis of prognostic genes. (E, F) LASSO coefficient profiles and cross-validation. (G) Kaplan-Meier OS curves for the high- and low-risk groups. (H) Risk score distribution, survival status, and expression patterns of the four signature genes. (I, J) ROC analyses in the TCGA training and GSE17536 external validation cohorts.

Figure 3. Construction and clinical evaluation of the prognostic nomogram in CRC. (A) Nomogram for predicting 1-, 3-, and 5-year OS. (B) ROC curves comparing the prognostic performance of the risk score and clinicopathological variables. (C, D) Univariate and multivariate Cox regression analyses. (E) Time-dependent C-indices of prognostic indicators. (F) Decision curve analysis of the evaluated prediction models.

Figure 4. Immune-associated characteristics and somatic mutation profiles of the CRC risk groups. (A) Comparison of immune cell infiltration between risk groups using CIBERSORT. (B) Differences in immune-related signatures and computational scores between risk groups. (C, D) Somatic mutation-associated pathway alterations in the high- and low-risk groups, respectively. (E, F) Somatic mutation landscapes of the low- and high-risk groups, respectively.

Figure 5. Expression patterns and clinical significance of SLC35D1 in CRC. (A) Single-cell annotation of the GSE166555 dataset. (B) Single-cell expression distribution of SLC35D1. (C) SLC35D1 expression in paired CRC and normal tissues.

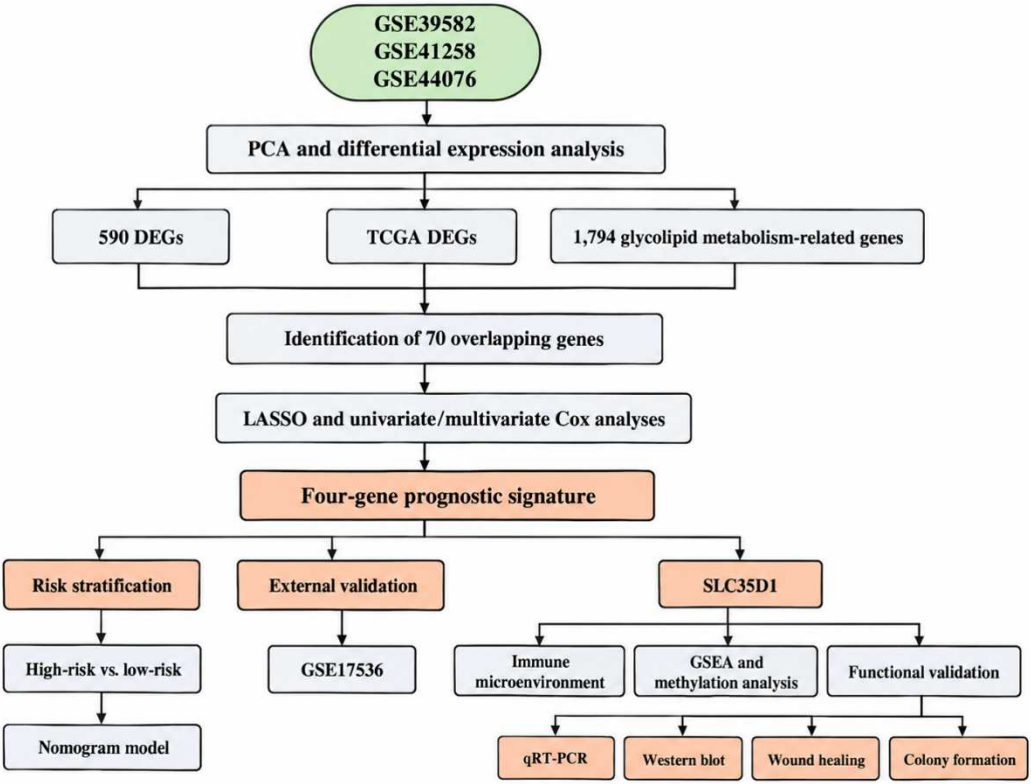
(D) ROC analysis of individual biomarkers and the four-gene signature. (E) Kaplan-Meier overall survival analysis according to SLC35D1 expression. (F-H) Associations of SLC35D1 expression with pathological T stage, overall pathological stage, and M stage, respectively. Pan-cancer expression patterns of SLC35D1 are shown in the central expression panel.

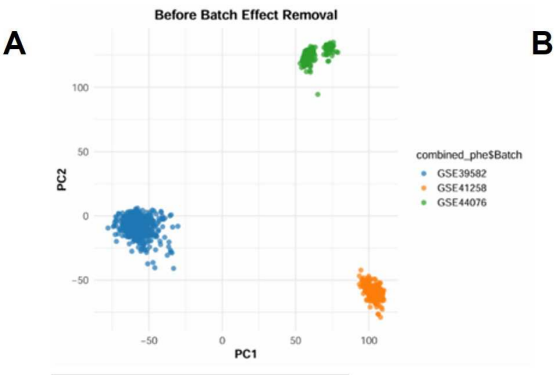
Figure 6. Associations between SLC35D1 expression and immune cell infiltration in CRC. (A) Relative proportions of infiltrating immune cell populations estimated using CIBERSORT. (B) Comparison of immune cell infiltration between the SLC35D1 expression groups. (C) Correlation analysis of SLC35D1 expression with immune cell subsets. (D-G) Correlations of SLC35D1 expression with natural killer cells, M1 macrophages, plasma cells, and naïve B cells, respectively.

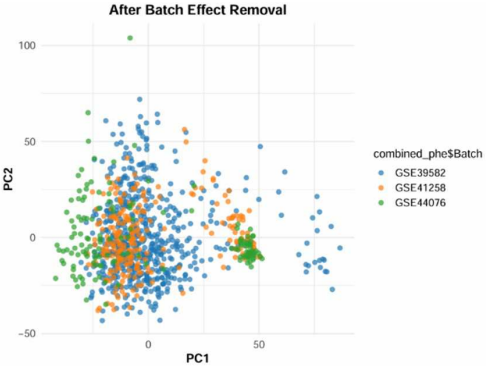
Figure 7. Functional enrichment analysis of SLC35D1-associated genes in CRC. (A) Gene Ontology (GO) enrichment analysis. (B) Kyoto Encyclopedia of Genes and Genomes (KEGG) pathway enrichment analysis. (C) Gene set enrichment analysis (GSEA). (D) Chord diagram illustrating associations between genes and enriched GO terms.

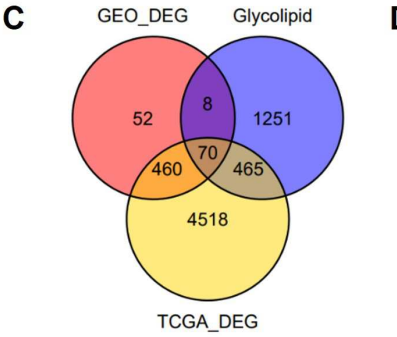
Figure 8. Associations of SLC35D1 expression with predicted drug responses and DNA methylation in CRC. (A-D) Predicted responses to 5-fluorouracil, dasatinib, docetaxel, and teniposide, respectively, in the SLC35D1 expression groups. (E) Correlation between overall SLC35D1 methylation and mRNA expression. (F, G) Correlations of SLC35D1 expression with DNA methylation at CpG sites cg09861436 and cg14626797, respectively.

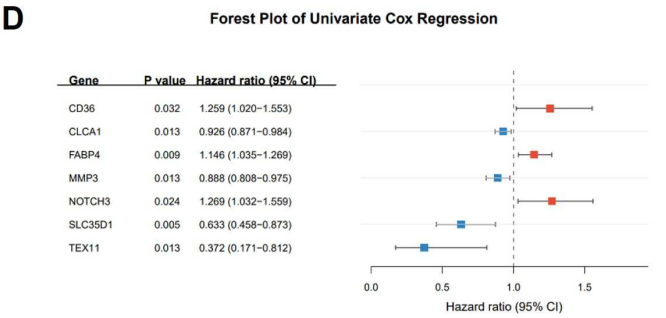
Figure 9. Effects of SLC35D1 overexpression on migration-related and clonogenic phenotypes in CRC cells. (A, B) Basal SLC35D1 mRNA and protein expression in CRC and control cells. (C, D) Western blot validation of SLC35D1 overexpression in HCT116 and LOVO cells, respectively. (E, F) Wound-healing assays in HCT116 and LOVO cells, respectively. (G) Representative colony formation images of HCT116 and LOVO cells. (H) Quantification of colony formation in HCT-116 and LOVO cells.

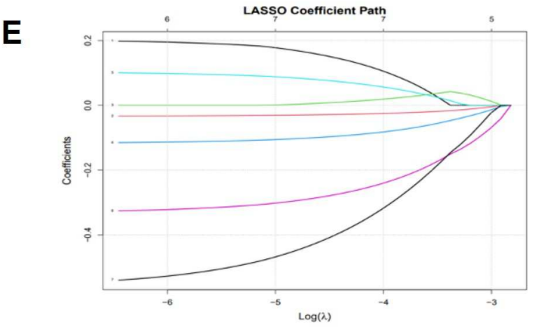

GSE39582
GSE41258
GSE44076
PCA and differential expression analysis
590 DEGs
TCGA DEGs
1,794 glycolipid metabolism-related genes
Identification of 70 overlapping genes
LASSO and univariate/multivariate Cox analyses
Four-gene prognostic signature
Risk stratification
External validation
SLC35D1
High-risk vs. low-risk
GSE17536
Immune microenvironment
GSEA and methylation analysis
Functional validation
Nomogram model
qRT-PCR
Western blot
Wound healing
Colony formation

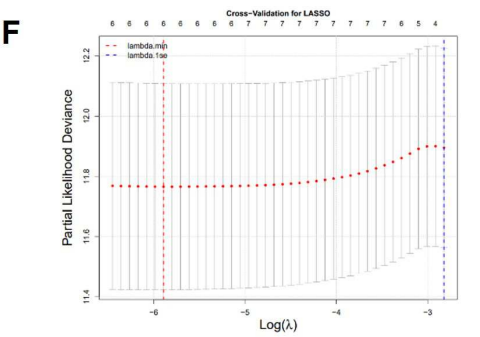

A
Before Batch Effect Removal
PC2
PC1
combined_phe$Batch
GSE39582
GSE41258
GSE44076

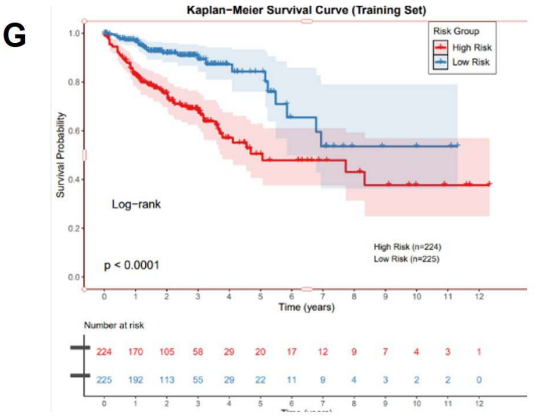

B
After Batch Effect Removal
PC2
PC1
combined_phe$Batch
GSE39582
GSE41258
GSE44076

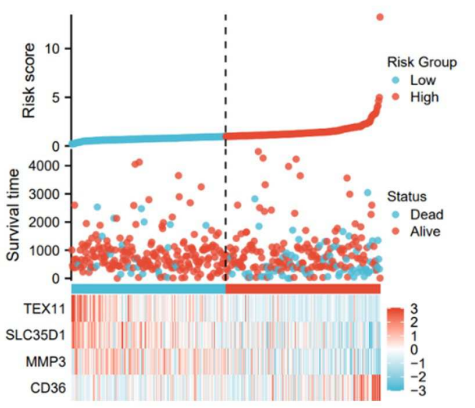

C
GEO_DEG
Glycolipid
TCGA_DEG
52
8
1251
70
460
465
4518

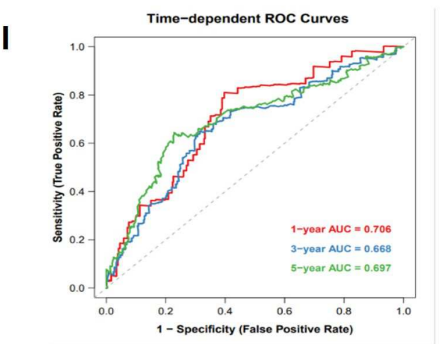

D
Forest Plot of Univariate Cox Regression
Gene P value Hazard ratio (95% CI)
CD36 0.032 1.259 (1.020−1.553)
CLCA1 0.013 0.926 (0.871−0.984)
FABP4 0.009 1.146 (1.035−1.269)
MMP3 0.013 0.888 (0.808−0.975)
NOTCH3 0.024 1.269 (1.032−1.559)
SLC35D1 0.005 0.633 (0.458−0.873)
TEX11 0.013 0.372 (0.171−0.812)
Hazard ratio (95% CI)

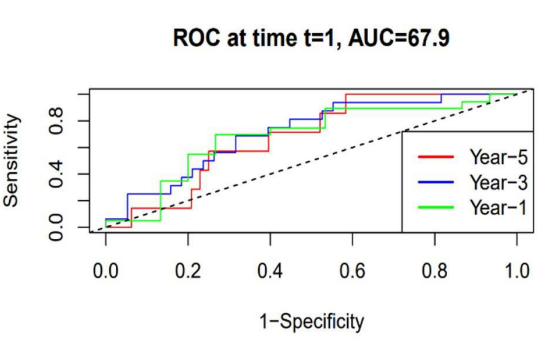

E
LASSO Coefficient Path
Coefficients
Log(λ)

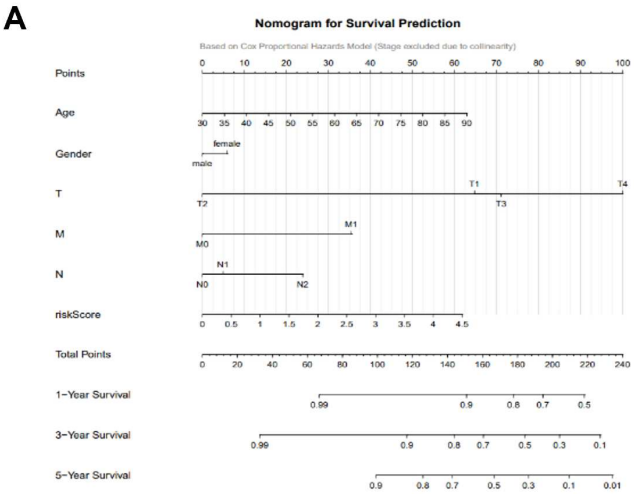

F
Cross-Validation for LASSO
lambda.min
lambda.1se
Partial Likelihood Deviance
Log(λ)

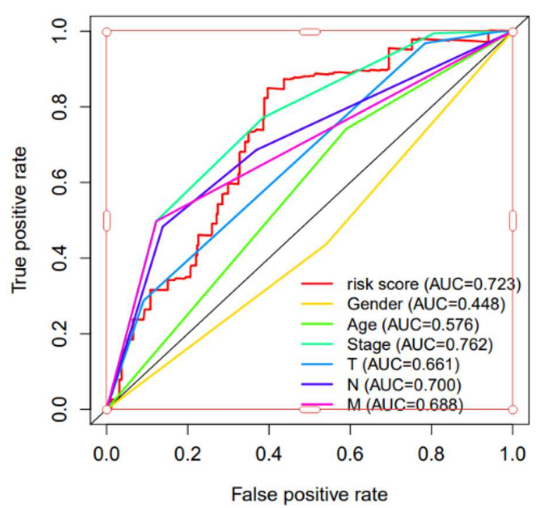

G
Kaplan−Meier Survival Curve (Training Set)
Risk Group
High Risk
Low Risk
Survival Probability
Log−rank
p < 0.0001
High Risk (n=224)
Low Risk (n=225)
Time (years)
Number at risk
224 170 105 58 29 20 17 12 9 7 4 3 1
225 192 113 55 29 22 11 9 4 3 2 2 0

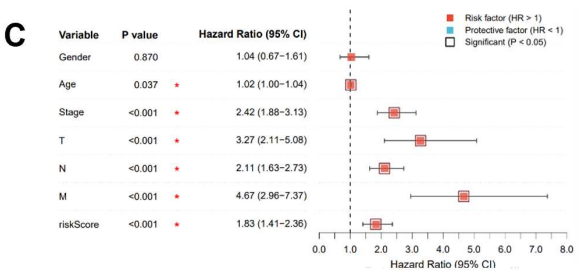

H
Risk score
Risk Group
Low
High
Survival time
Status
Dead
Alive
TEX11
SLC35D1
MMP3
CD36

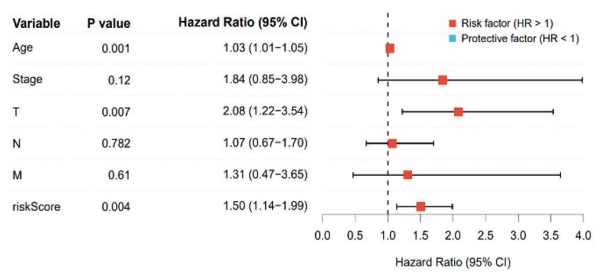

I
Time−dependent ROC Curves
Sensitivity (True Positive Rate)
1 − Specificity (False Positive Rate)
1−year AUC = 0.706
3−year AUC = 0.668
5−year AUC = 0.697

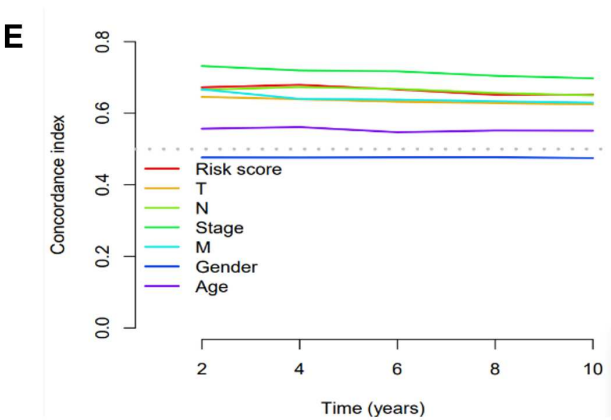

J
ROC at time t=1, AUC=67.9
Sensitivity
1−Specificity
Year−5
Year−3
Year−1

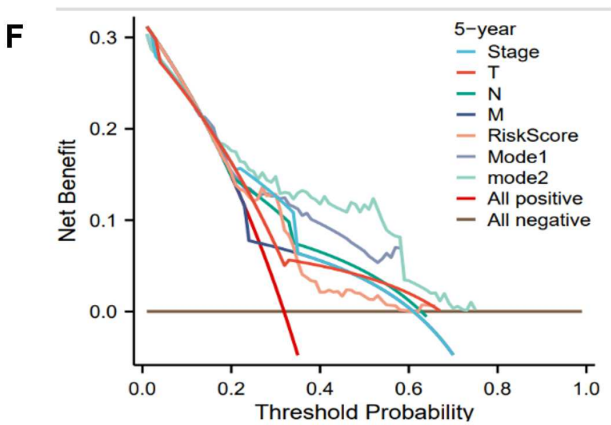

A
Nomogram for Survival Prediction
Based on Cox Proportional Hazards Model (Stage excluded due to collinearity)
Points
Age
Gender
female
male
T
T1
T2
T3
T4
M
M0
M1
N
N0
N1
N2
riskScore
Total Points
1−Year Survival
3−Year Survival
5−Year Survival

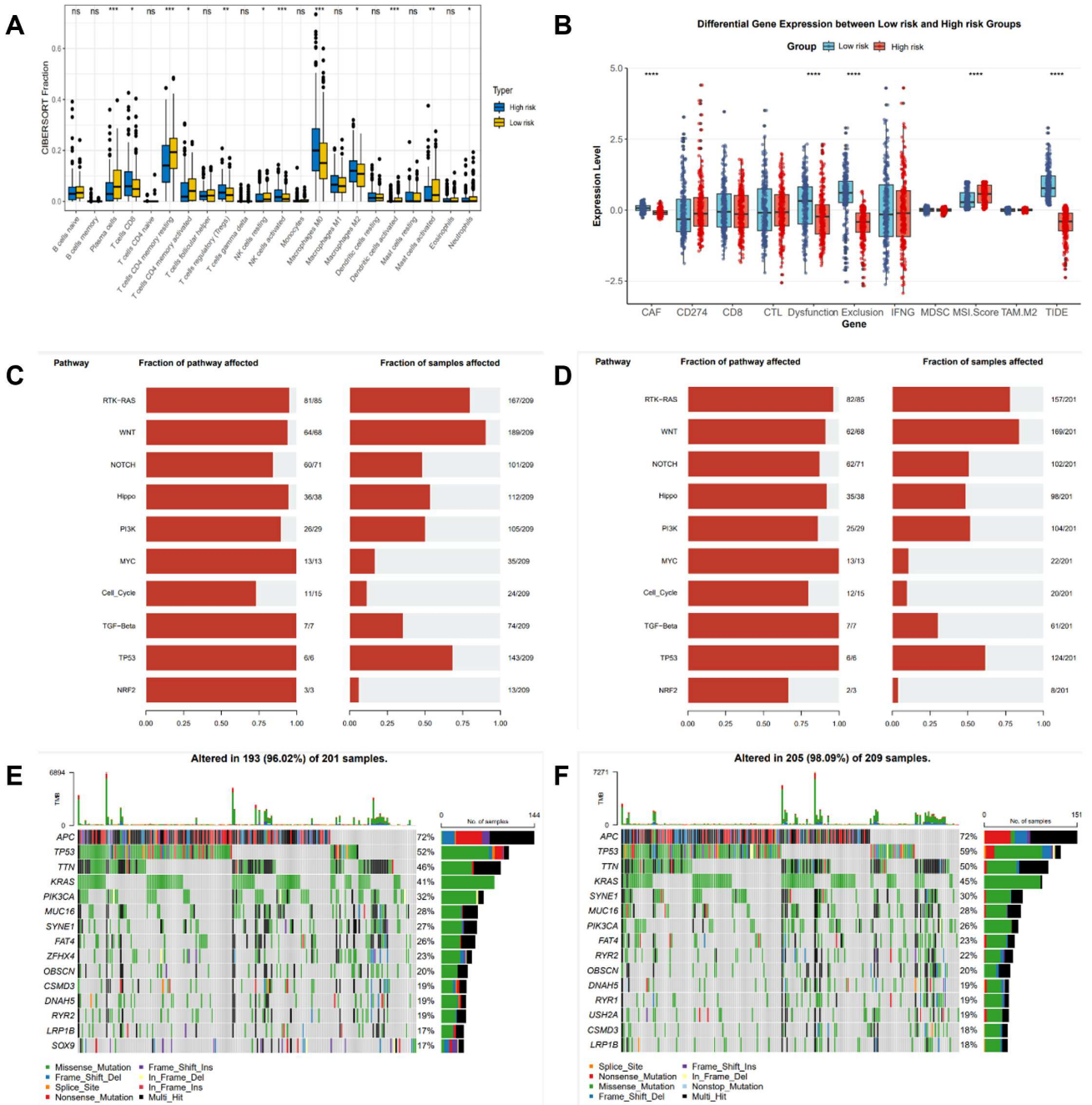

B
True positive rate
False positive rate
risk score (AUC=0.723)
Gender (AUC=0.448)
Age (AUC=0.576)
Stage (AUC=0.762)
T (AUC=0.661)
N (AUC=0.700)
M (AUC=0.688)

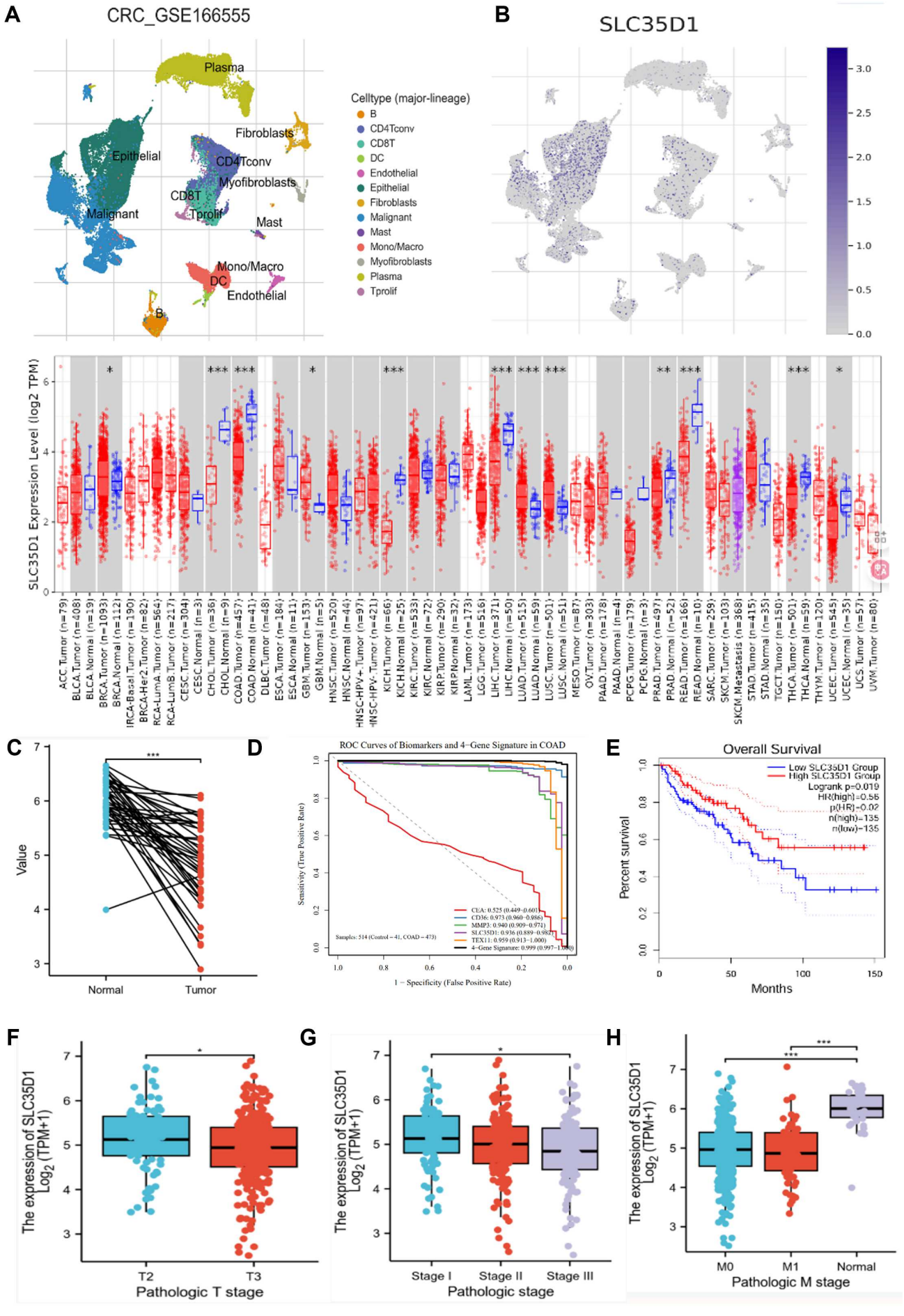

C
Variable
P value
Hazard Ratio (95% CI)
Risk factor (HR > 1)
Protective factor (HR < 1)
Significant (P < 0.05)
Gender 0.870 1.04 (0.67−1.61)
Age 0.037 * 1.02 (1.00−1.04)
Stage <0.001 * 2.42 (1.88−3.13)
T <0.001 * 3.27 (2.11−5.08)
N <0.001 * 2.11 (1.63−2.73)
M <0.001 * 4.67 (2.96−7.37)
riskScore <0.001 * 1.83 (1.41−2.36)
Hazard Ratio (95% CI)

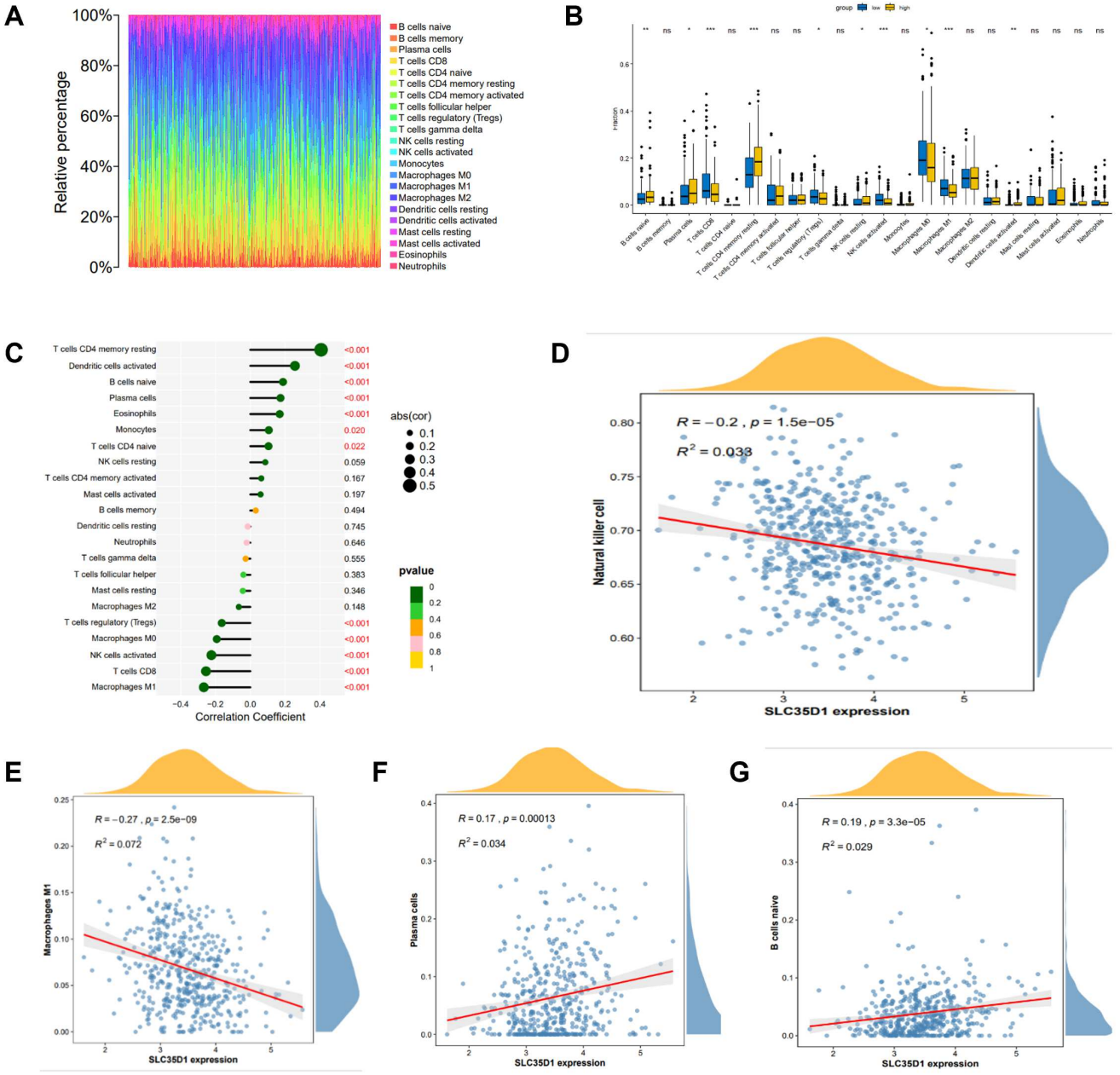

D
Variable
P value
Hazard Ratio (95% CI)
Risk factor (HR > 1)
Protective factor (HR < 1)
Age 0.001 1.03 (1.01−1.05)
Stage 0.12 1.84 (0.85−3.98)
T 0.007 2.08 (1.22−3.54)
N 0.782 1.07 (0.67−1.70)
M 0.61 1.31 (0.47−3.65)
riskScore 0.004 1.50 (1.14−1.99)
Hazard Ratio (95% CI)

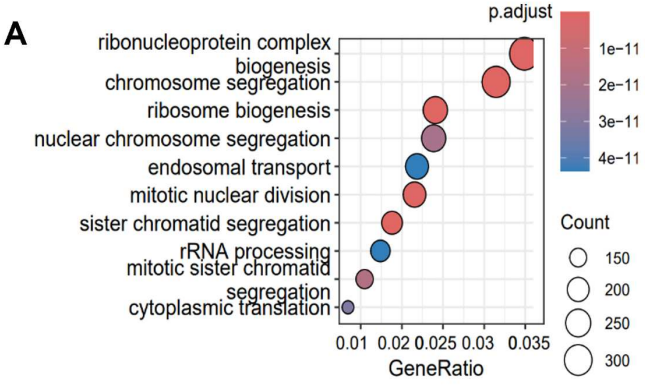

E
Concordance index
Time (years)
Risk score
T
N
Stage
M
Gender
Age

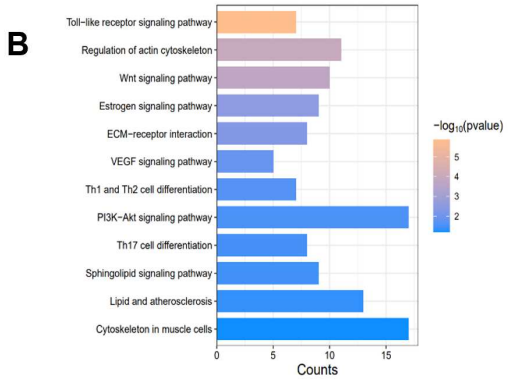

F
Net Benefit
Threshold Probability
5−year
Stage
T
N
M
RiskScore
Mode1
mode2
All positive
All negative

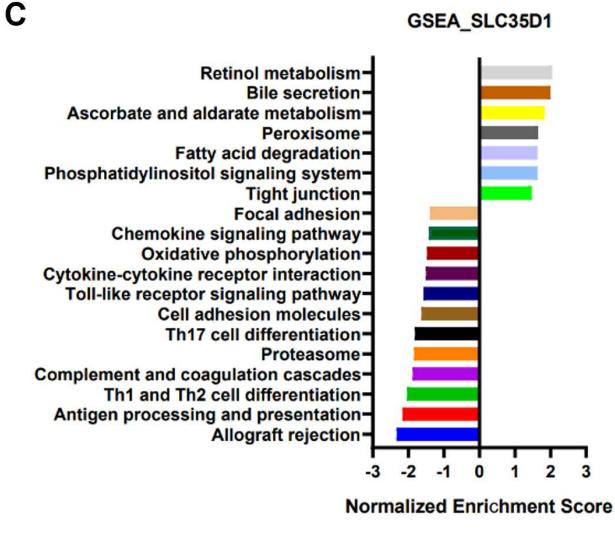

A
CIBERSORT Fraction
Typer
High risk
Low risk
B cells naive
B cells memory
Plasma cells
T cells CD8
T cells CD4 naive
T cells CD4 memory resting
T cells CD4 memory activated
T cells follicular helper
T cells regulatory (Tregs)
T cells gamma delta
NK cells resting
NK cells activated
Monocytes
Macrophages M0
Macrophages M1
Macrophages M2
Dendritic cells resting
Dendritic cells activated
Mast cells resting
Mast cells activated
Eosinophils
Neutrophils
B
Differential Gene Expression between Low risk and High risk Groups
Group
Low risk
High risk
Expression Level
CAF
CD274
CD8
CTL
Dysfunction
Exclusion
IFNG
MDSC
MSI.Score
TAM.M2
TIDE
Gene
C
Pathway
Fraction of pathway affected
Fraction of samples affected
RTK-RAS
WNT
NOTCH
Hippo
PI3K
MYC
Cell_Cycle
TGF-Beta
TP53
NRF2
81/85
64/68
60/71
36/38
26/29
13/13
11/15
7/7
6/6
3/3
167/209
189/209
101/209
112/209
105/209
35/209
24/209
74/209
143/209
13/209
D
Pathway
Fraction of pathway affected
Fraction of samples affected
RTK-RAS
WNT
NOTCH
Hippo
PI3K
MYC
Cell_Cycle
TGF-Beta
TP53
NRF2
82/85
62/68
62/71
35/38
25/29
13/13
12/15
7/7
6/6
2/3
157/201
169/201
102/201
98/201
104/201
22/201
20/201
61/201
124/201
8/201
E
Altered in 193 (96.02%) of 201 samples.
TMB
No. of samples
APC 72%
TP53 52%
TTN 46%
KRAS 41%
PIK3CA 32%
MUC16 28%
SYNE1 27%
FAT4 26%
ZFHX4 23%
OBSCN 20%
CSMD3 19%
DNAH5 19%
RYR2 19%
LRP1B 17%
SOX9 17%
Missense_Mutation
Frame_Shift_Ins
Frame_Shift_Del
In_Frame_Del
Splice_Site
In_Frame_Ins
Nonsense_Mutation
Multi_Hit
F
Altered in 205 (98.09%) of 209 samples.
TMB
No. of samples
APC 72%
TP53 59%
TTN 50%
KRAS 45%
SYNE1 30%
MUC16 28%
PIK3CA 26%
FAT4 23%
RYR2 22%
OBSCN 20%
DNAH5 19%
RYR1 19%
USH2A 19%
CSMD3 18%
LRP1B 18%
Splice_Site
Frame_Shift_Ins
Nonsense_Mutation
In_Frame_Del
Missense_Mutation
Nonstop_Mutation
Frame_Shift_Del
Multi_Hit

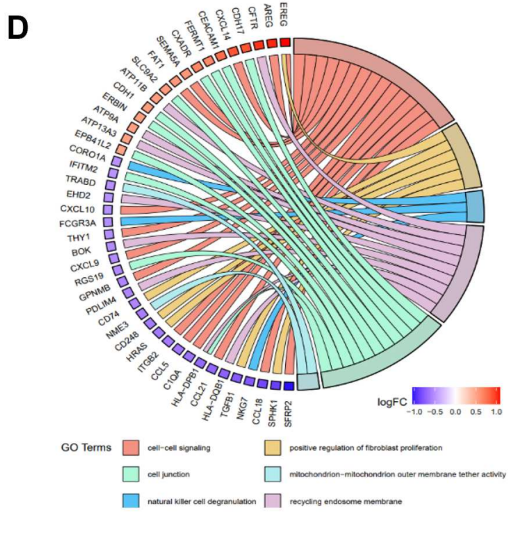

A
CRC_GSE166555
Plasma
Fibroblasts
Epithelial
CD4Tconv
Myofibroblasts
CD8T
Tprolif
Malignant
Mast
Mono/Macro
DC
Endothelial
B
Celltype (major-lineage)
B
CD4Tconv
CD8T
DC
Endothelial
Epithelial
Fibroblasts
Malignant
Mast
Mono/Macro
Myofibroblasts
Plasma
Tprolif
B
SLC35D1
3.0
2.5
2.0
1.5
1.0
0.5
0.0
SLC35D1 Expression Level (log2 TPM)
C
Value
Normal
Tumor
D
ROC Curves of Biomarkers and 4−Gene Signature in COAD
Sensitivity (True Positive Rate)
1 − Specificity (False Positive Rate)
CLIA: 0.525 (0.449−0.601)
CD36: 0.973 (0.960−0.986)
MMP3: 0.940 (0.909−0.971)
SLC35D1: 0.936 (0.889−0.983)
TEX11: 0.959 (0.913−1.000)
4−Gene Signature: 0.999 (0.997−1.000)
Samples: 514 (Control = 41, COAD = 473)
E
Overall Survival
Low SLC35D1 Group
High SLC35D1 Group
Logrank p=0.019
HR(high)=0.56
p(HR)=0.02
n(high)=135
n(low)=135
Percent survival
Months
F
The expression of SLC35D1 Log2 (TPM+1)
T2
T3
Pathologic T stage
G
The expression of SLC35D1 Log2 (TPM+1)
Stage I
Stage II
Stage III
Pathologic stage
H
The expression of SLC35D1 Log2 (TPM+1)
M0
M1
Normal
Pathologic M stage

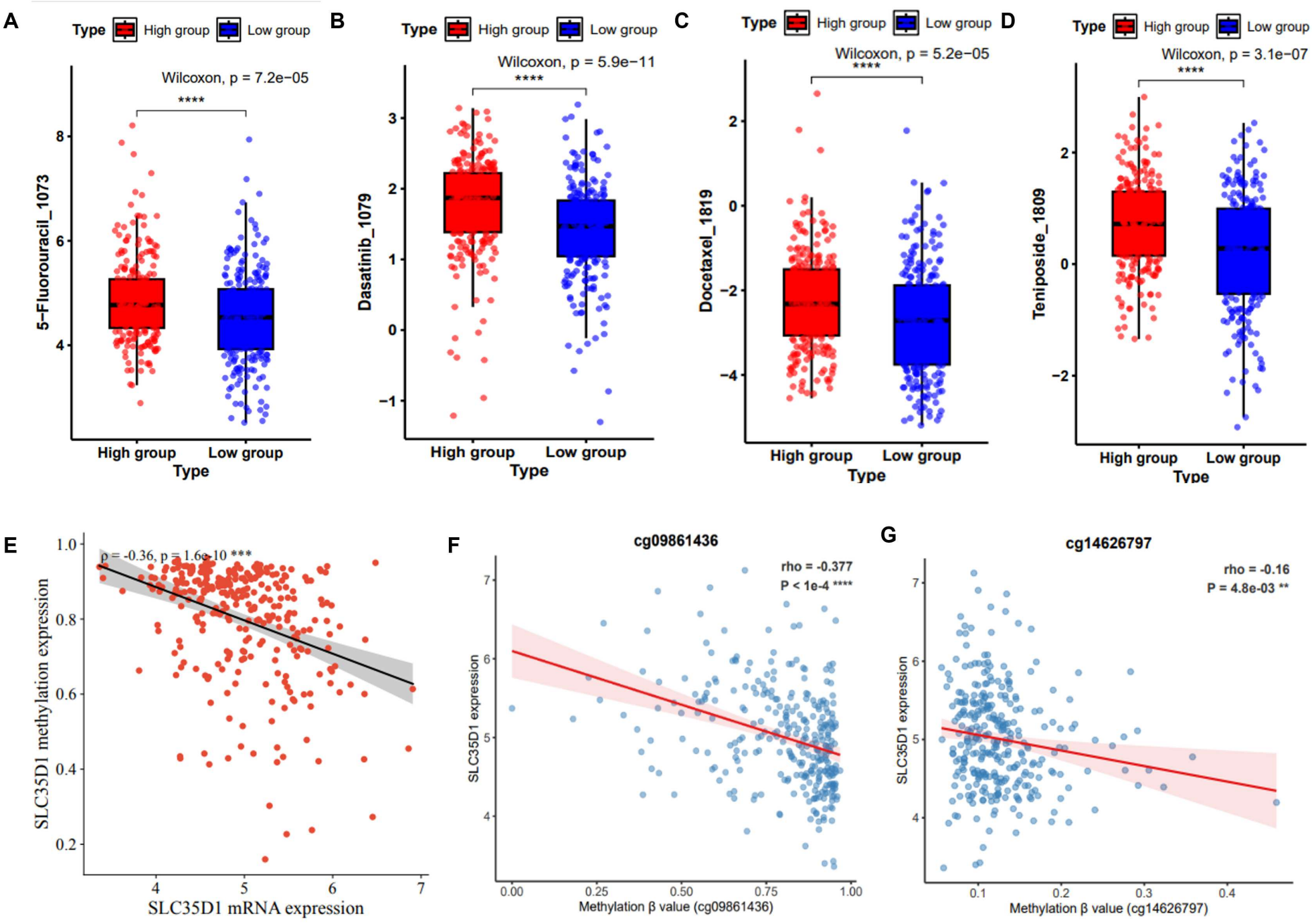

A
Relative percentage
100%
80%
60%
40%
20%
0%
B cells naive
B cells memory
Plasma cells
T cells CD8
T cells CD4 naive
T cells CD4 memory resting
T cells CD4 memory activated
T cells follicular helper
T cells regulatory (Tregs)
T cells gamma delta
NK cells resting
NK cells activated
Monocytes
Macrophages M0
Macrophages M1
Macrophages M2
Dendritic cells resting
Dendritic cells activated
Mast cells resting
Mast cells activated
Eosinophils
Neutrophils
B
group low high
Fraction
C
T cells CD4 memory resting <0.001
Dendritic cells activated <0.001
B cells naive <0.001
Plasma cells <0.001
Eosinophils <0.001
Monocytes 0.020
T cells CD4 naive 0.022
NK cells resting 0.059
T cells CD4 memory activated 0.167
Mast cells activated 0.197
B cells memory 0.494
Dendritic cells resting 0.745
Neutrophils 0.646
T cells gamma delta 0.555
T cells follicular helper 0.383
Mast cells resting 0.346
Macrophages M2 0.148
T cells regulatory (Tregs) <0.001
Macrophages M0 <0.001
NK cells activated <0.001
T cells CD8 <0.001
Macrophages M1 <0.001
abs(cor)
0.1
0.2
0.3
0.4
0.5
pvalue
0
0.2
0.4
0.6
0.8
1
−0.4 −0.2 0.0 0.2 0.4
Correlation Coefficient
D
R = −0.2 , p = 1.5e−05
R² = 0.038
Natural killer cell
SLC35D1 expression
E
R = −0.27 , p = 2.5e−09
R² = 0.072
Macrophages M1
SLC35D1 expression
F
R = 0.17 , p = 0.00013
R² = 0.034
Plasma cells
SLC35D1 expression
G
R = 0.19 , p = 3.3e−05
R² = 0.029
B cells naive
SLC35D1 expression

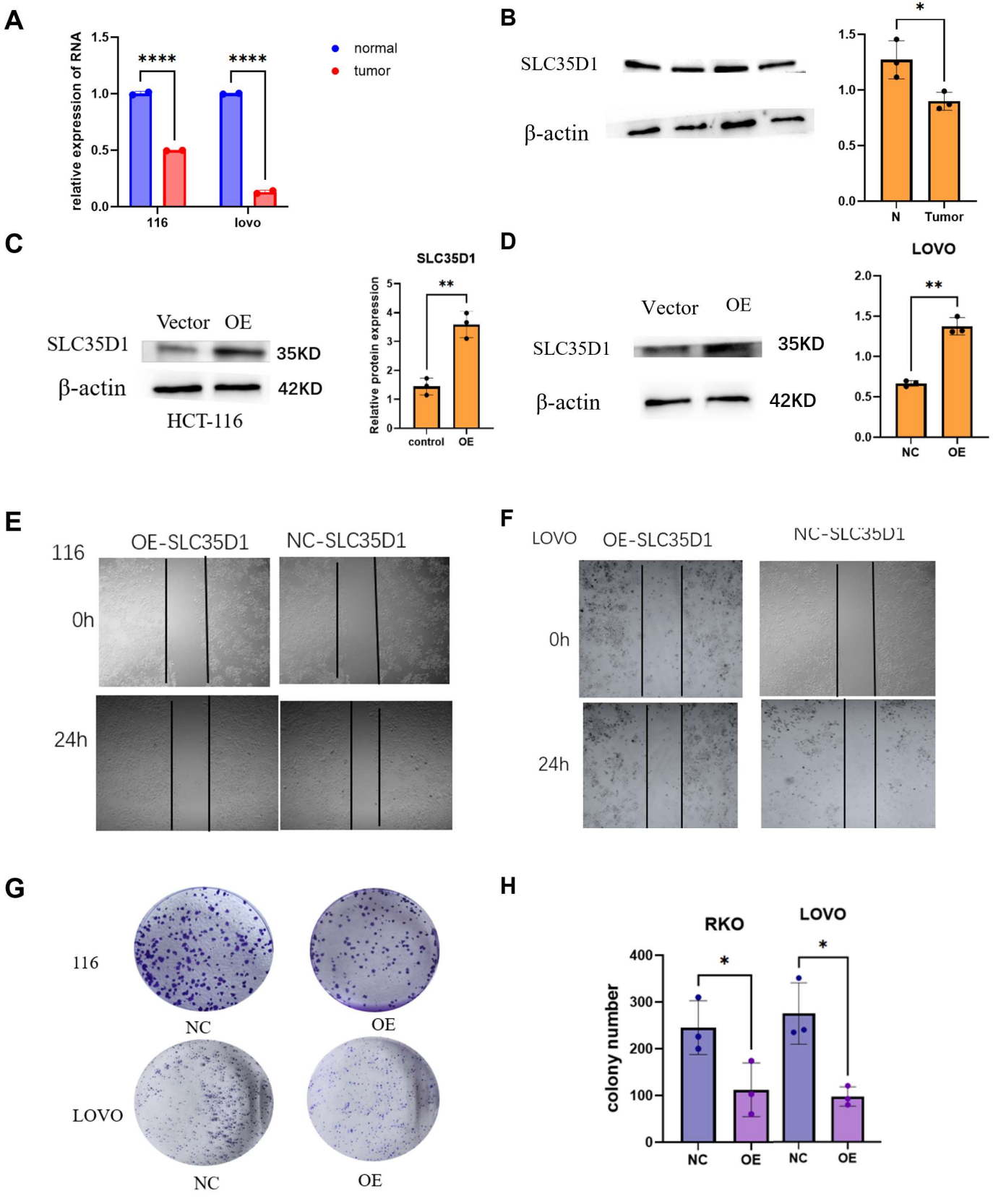

A
p.adjust
1e−11
2e−11
3e−11
4e−11
ribonucleoprotein complex biogenesis
chromosome segregation
ribosome biogenesis
nuclear chromosome segregation
endosomal transport
mitotic nuclear division
sister chromatid segregation
rRNA processing
mitotic sister chromatid segregation
cytoplasmic translation
0.01 0.02 0.025 0.03 0.035
GeneRatio
Count
150
200
250
300


B
Toll−like receptor signaling pathway
Regulation of actin cytoskeleton
Wnt signaling pathway
Estrogen signaling pathway
ECM−receptor interaction
VEGF signaling pathway
Th1 and Th2 cell differentiation
PI3K−Akt signaling pathway
Th17 cell differentiation
Sphingolipid signaling pathway
Lipid and atherosclerosis
Cytoskeleton in muscle cells
0 5 10 15
Counts
−log10(pvalue)
5
4
3
2


C
GSEA_SLC35D1
Retinol metabolism
Bile secretion
Ascorbate and aldarate metabolism
Peroxisome
Fatty acid degradation
Phosphatidylinositol signaling system
Tight junction
Focal adhesion
Chemokine signaling pathway
Oxidative phosphorylation
Cytokine-cytokine receptor interaction
Toll-like receptor signaling pathway
Cell adhesion molecules
Th17 cell differentiation
Proteasome
Complement and coagulation cascades
Th1 and Th2 cell differentiation
Antigen processing and presentation
Allograft rejection
-3 -2 -1 0 1 2 3
Normalized Enrichment Score


D
EREG
AREG
CFTR
CDH17
CXCL14
CEACAM1
FERMT1
CYP4X1
SEMA5A
FAT1
SLC9A2
ATP1B1
CDH1
ERBIN
ATP6IA
ATP13A3
EPB41L2
CORO1A
IFITM2
TRABD
EHD2
CXCL10
FCGR3A
THY1
BOK
CXCL9
RGS19
GPNMB
PDLIM4
CD74
NMB
CD248
HPAS
ITGB2
CCL5
C1QA
HLA-DPB1
CCL21
HLA-DQB1
TGFB1
NKG7
CCL18
SPHK1
SRRP2
logFC
−1.0 −0.5 0.0 0.5 1.0
GO Terms
cell−cell signaling
cell junction
natural killer cell degranulation
positive regulation of fibroblast proliferation
mitochondrion−mitochondrion outer membrane tether activity
recycling endosome membrane


A
Type
High group
Low group
Wilcoxon, p = 7.2e−05
****
5−Fluorouracil_1073
High group
Low group
Type
B
Type
High group
Low group
Wilcoxon, p = 5.9e−11
****
Dasatinib_1079
High group
Low group
Type
C
Type
High group
Low group
Wilcoxon, p = 5.2e−05
****
Docetaxel_1819
High group
Low group
Type
D
Type
High group
Low group
Wilcoxon, p = 3.1e−07
****
Teniposide_1809
High group
Low group
Type
E
ρ = -0.36, p = 1.6e-10 ***
SLC35D1 methylation expression
SLC35D1 mRNA expression
F
cg09861436
rho = -0.377
P < 1e-4 ****
SLC35D1 expression
Methylation β value (cg09861436)
G
cg14626797
rho = -0.16
P = 4.8e-03 **
SLC35D1 expression
Methylation β value (cg14626797)


A
relative expression of RNA
1.5
1.0
0.5
0.0
****
****
normal
tumor
116
lovo
B
SLC35D1
β-actin
*
1.5
1.0
0.5
0.0
N
Tumor
C
Vector
OE
SLC35D1
35KD
β-actin
42KD
HCT-116
SLC35D1
**
Relative protein expression
5
4
3
2
1
0
control
OE
D
Vector
OE
SLC35D1
35KD
β-actin
42KD
LOVO
**
2.0
1.5
1.0
0.5
0.0
NC
OE
E
116
OE-SLC35D1
NC-SLC35D1
0h
24h
F
LOVO
OE-SLC35D1
NC-SLC35D1
0h
24h
G
116
NC
OE
LOVO
NC
OE
H
RKO
LOVO
*
*
colony number
400
300
200
100
0
NC
OE
NC
OE